Bachelor's Thesis in Chemical Physics

Study of the vibronic mixing in chlorophylls with multidimensional spectroscopy

by

Ignacio Martínez Casasús

Contents

1 Acknowledgments

First of all, I would like to express the utmost gratitude and appreciation to my supervisor, Donatas. You have been always there since the very beginning of my life in Lund, even until late hours on the night. You have showed me how the good science is done: with resilience, persistence, criticism, honesty and the most meticulous care. I will never forget you, and I will always feel very fortunate to have begun and traveled this exciting research journey at your side.

This thesis would not have been possible without my dear mentor, Daniel. You have showed me the beauty of this world, pushing me to keep going when I needed it most. Both Sweden and Physics were, at the beginning, foreign for me; but you always made them feel like home. Thank you very much for your guidance and persistent help, I will never forget it.

Another big thanks goes to you, Eglė. You have been an inestimable help, dedicating an incalculable amount of time to me. From the lab work to the data analysis, you have been always there. Without your careful explanations about all the scientific basis of coherences, this project would have not been possible.

Thank you very much to you, Pierre-Adrien. You have been an amazing office colleague, and I feel like you have been like my older brother during this time in Sweden. Always with a helping hand, encouraging me to learn and to push further new skills. I will always appreciate that.

Thanks to David. You, in the distance, have been a crucial part of the development of this work. Your help with the data analysis and your theoretical guide have been essential support points for me, and I will be always grateful with you for that.

Special thanks to my professors at the Universidad Complutense de Madrid too, particularly to José and Juan Enrique. I discovered this new *quantum* world with your lectures, and it will remain in me forever thanks to your work. Thank you for being such a great inspiration to me.

I would like to say thank you to all the people on the Chemical-Physics division. To my group colleagues, Pavel and Lukas: you have become the best role-models for me; to Jens Uhlig, for unveiling me the world of Python; to all the PIs, whom I greatly admire; and to the rest of the incredible people that have accompany me through this path.

My lovely Claudia, thank you for being by my side all of this time. Your support, help, company, and love are the most valuable things on this world. Not only this thesis, but the whole degree and what I am now wouldn't have been possible without you. I deeply admire you, Claudia, and I'm looking forward to living the rest of my life with you.

My dear parents, Maria Jesús and Luis, you have taught me to be the way I am, and you have given me everything you have. If I can pursuit my dreams as I do, if I can enjoy living as I do, it is just thanks to you. My big brother, Luis, you are the best brother that one can have. For as long as I can remember, you have always been the person I wanted to be when I grew up. And believe me, that will never change. And of course, to Elena, I could not be happier than with you as a part of our family.

Special thanks too to all my friends and relatives who take care of me from the distance; and to the "Cooler People", who has become an essential part of my life in such a short time. I greatly appreciate you all.

2 Abstract

Chlorophylls comprise one of the most important families of molecules for the photosynthetic process. Chlorophyll-like molecules have been classically interpreted under the Gouterman model, being thought to feature two independent transitions, $Q_y(S_1)$ and $Q_x(S_2)$. Recent studies on the matter provided a new interpretation, assuming these states to feature strong vibronic coupling and to be inseparably mixed. Experimental study of vibronic mixing can be done with non-linear spectroscopy techniques that can create and record superpositions of states, the so-called "coherences". These coherences, when excited via vibronically coupled transitions, represent a direct observation of vibronic mixing phenomena. Polarization-controlled two-dimensional electronic spectroscopy is performed on chlorophyll a at cryogenic (77 K) temperature, followed by a complex analysis to the oscillatory signals, unveiling vibronic coupling in the most common member of the chlorophyll family.

3 Introduction

Chlorophyllides and chlorophyll-like molecules play a major role in photosynthesis. The presence of vibronic mixing in these molecules was purposed by Reimers et al. [1], who developed a complete vibronic coupling model for them. The presence of vibronic coupling in chlorophyll molecules is not generalized yet, although evidences of it have been found on chlorophyll a (Chl a) [2] and its direct observation has been made in chlorophyll c_1 (Chl c_1) [3].

The study of vibronic mixing is carried out with polarized-controlled two-dimensional electronic spectroscopy (2DES). 2DES is a cutting-edge non-linear spectroscopy technique that can create a superposition of states in an ensemble of molecules. These superpositions are called "coherences", and they manifest as oscillations in 2DES experiments. The origin of these coherences is diverse, as they can originate from a vibrational, electronic or vibronic superposition of states. With double-crossed (DC) polarization control unwanted signals can be selectively suppressed, which makes it possible to observe only electronic coherences or coherences excited via vibronically coupled states. With the proper experimental set-up and analysis, direct observation of these coherences excited via vibronically coupled states can be done.

Here, the methodology of Bukartė et al. [3] is applied to Chl a, a more common system than Chl c_1. The aim of the project is to observe and characterize vibronic mixing in an easy-to-obtain molecule and the most common of the chlorophylls family. This would allow a generalization of the mixing phenomenon leading, at the same time, the open path for new and deeper studies of the matter.

The work is performed is in the framework of an end-of-degree thesis developed in Lund University within the dates of 2020-09-01 and 2021-01-17. The thesis is organized as follows. Chapter 3 provides the theoretical background needed to understand the experiments, describing 2DES, its polarization-control implementation and the coherences signals pursued. In Chapter 4, the experimental considerations, the system under study, and analysis methodology are described. Chapter 5 contains the main experimental results, including the principal 2DES graphs and the so-called "beating maps". Finally, in chapter 6 the conclusions of the work are given.

4 Coherences and two-dimensional electronic spectroscopy

4.1 Two-dimensional electronic spectroscopy. Description of the technique

2DES is a time-resolved spectroscopy that measures the full nonlinear polarization of a quantum system in third-order regarding the field–matter interaction [4, 5]. One intuitive way to understand 2DES is as non-linear spectroscopy which is an extension of the so-called transient absorption (TA). The application of more than one pulse is necessary for achieving time resolution in any spectroscopic technique.

In transient absorption, a first pulse, the so-called "pump" pulse, perturbs the sample at t=0. The second one, the so-called "probe" pulse, crosses the perturbed sample with some time delay with respect to the pump pulse [6]. The time delay between pulses can be varied, allowing the probe pulse to measure the system's absorption at different time delays. By subtracting the system's absorption (without the pump pulse) from this signal, we can track the change in absorption due to the initial perturbation, and then identify the evolution of the system.

In 2DES, the pulse sequence applied to the system is more complex, and it is shown in the Figure 1. There are clearly three times intervals of interest [7]: The delay between the first and the second pulses, t_1, known as coherence time; the delay between the second and the third pulse, t_2, known as population time; and the time after the third pulse, t_3. The time axis, which we perform measurements on, is therefore defined by the delay between pulses.
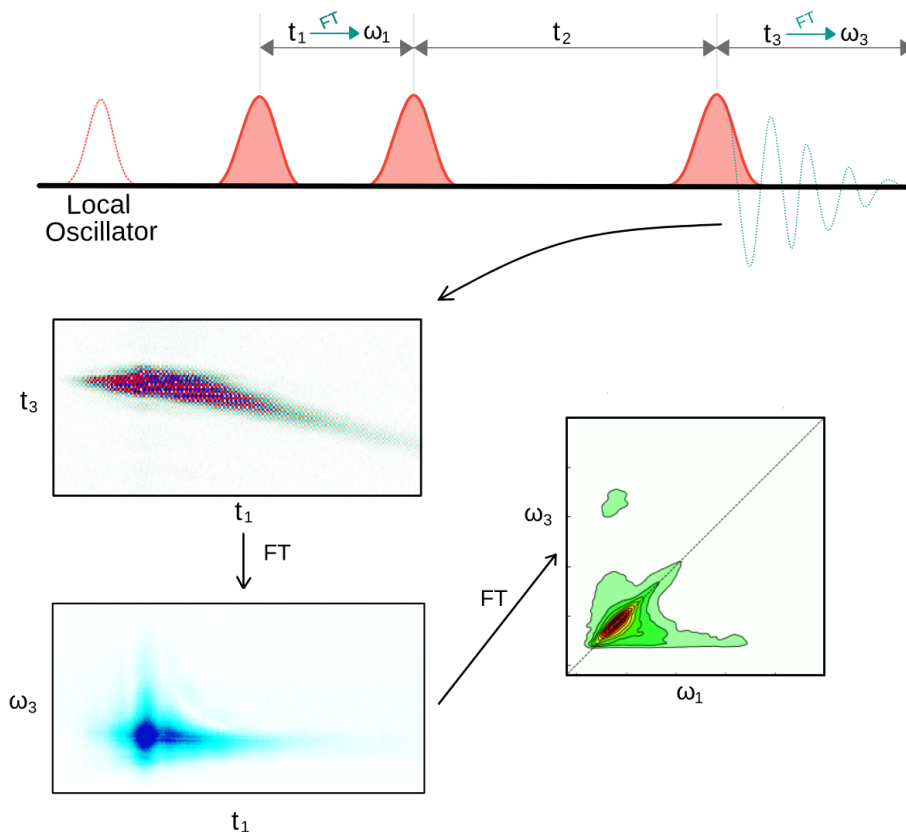

Figure 1: Top: pulse sequence for 2DES. Bottom: from the emitted electric field is possible to obtain the 2D map for a fixed t_2. The signal (top left rectangle) is heterodyne-detected in the CCD camera, with a spectrometer effectively performing a Fourier transform to recover ω_3. Then, another FT along t_1 finally allows us to construct the 2D map.

The two first pulses act as pump pulses, giving the system time to evolve during the population time. After t_2, the system is probed with the third pulse, which induces the third-order polarization on it. Finally, the system emits an electric field in a specific phase-matched direction, and heterodyned with the fourth pulse, called local oscillator (LO). This type of implementation of 2DES is often called "photon echo type".

2DES can reveal connections between optical excitation frequencies and frequencies of the signal emitted by the system [8]. To achieve this, a complete set of 2D spectra is recorded by the scan of t_1 and t_3 for different fixed t_2, obtaining signals of the type $S(\omega_1, t_2, \omega_3)$. The methodology applied to obtain frequencies from the scan of t_1 and t_3 is different in each case.

The detection frequencies, ω_3, are usually obtained via heterodyne-detected frequency-domain measurement, in which a spectrometer effectively performs the Fourier transform [7, 8]. The spectral interferometry provides a complete measurement of the complex electric field of the signal, E_{sig}, as a continuous function of frequency [9]. In order to be amplified, the signal field comes together with a reference field, the one of the local oscillator, E_{LO}. A stable relative time delay and phase between the signal and local oscillator are necessary to extract the signal.

To obtain the excitation frequencies, ω_1, the coherence time t_1 is scanned, and the Fourier transform methodology is applied. The signal obtained then has decent spectral and high temporal resolution.

As a summary, the third-order polarization is a function of three-time delays between pulses and, therefore, the signal obtained is a function of them too, $S(t_1, t_2, t_3)$. Spectral interferometry allows us to extract the detection frequencies directly on the spectrometer, obtaining $S(t_1, t_2, \omega_3)$. Then, the application of the FFT over t_1 recovers the excitation frequencies, and one two-dimensional spectrum from the signal $S(\omega_1, t_2, \omega_3)$ for a fixed t_2 can be obtained. The repetition of this process for a fixed number of t_2 points generates a full sequence of 2D spectra, in which the evolution of the system after the excitation (pump pulses) is recorded and can be studied along the different maps.

Given the sequence of pulses applied, this technique is mainly focused on the study of the third-order response of the system. The third-order polarization generated by the system will lead to the emission of an electric field in the direction given by the combination of the wave-vectors of the pulses, which are called $\vec{k_1}, \vec{k_2}, \vec{k_3}$. Then, the nonlinear signal will be emitted in several directions $\vec{k_s} = \pm\vec{k_1} \pm \vec{k_2} \pm \vec{k_3}$.

There are many third-order response functions possible and, with phase matching, some of them can be discriminated against the others [10]. The concept of phase-matching is illustrated in Figure 2, where the geometry of the input directions of the three laser beams is responsible for the directions in which nonlinear signals are emitted.
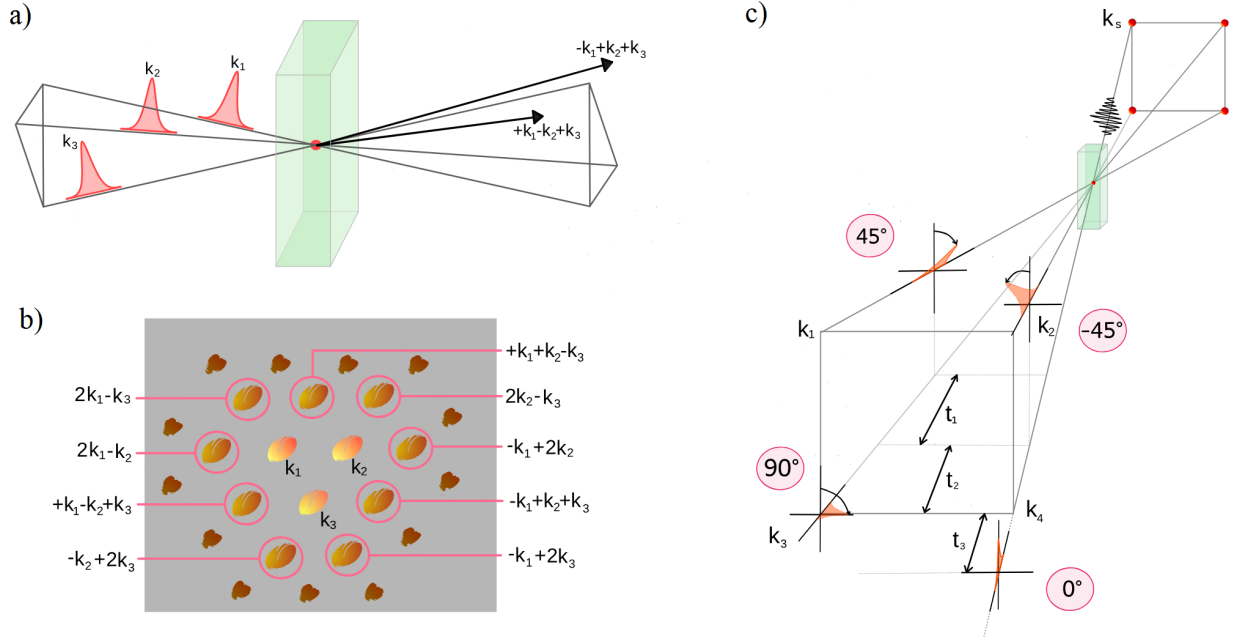
Figure 2: Illustration of phase-matching in multidimensional spectroscopy. a) One possible phase matching used, where three input beams with wavevectors, $\overrightarrow{k_1}$, $\overrightarrow{k_2}$ and $\overrightarrow{k_3}$ perturb the sample and then non-linear signals are emitted. Rephasing $-\overrightarrow{k_1} + \overrightarrow{k_2} + \overrightarrow{k_3}$ and non-rephasing $+\overrightarrow{k_1} - \overrightarrow{k_2} + \overrightarrow{k_3}$ are highlighted. b) Picture of the emitted fields. Several possibilities of phase matching for third order responses are highlighted. Moreover, it is also possible to observe weaker beams from higher-order responses. c) Phase-matching condition for the rephasing 2DES signal in the BOXCARS geometry. Note the specific polarization orientation of each pulse on the specific case of DC polarization-controlled 2DES. Both figures a) and b) are adapted from [10].

4.2 Experimental set-up

The 2DES experimental set up uses a femtosecond laser system called PHAROS (Light Conversion Ltd.), which is based on a Yb:KGW lasing medium. The central wavelength output of the laser is (1030 ± 10)nm. Therefore, it is necessary to employ non-linear optical systems to tune from the infrared wavelengths to the visible ones. A non-collinear parametric amplifier (NOPA) is employed for that, in order to produce pulses with the desired intensity on the desired wavelength. After the NOPA, the bluest part of the output beam is slightly cut by using a two prisms system. Then, the beam continues its path inside the "2D BOX", which is schematically represented in Figure 3.

Inside this box, the main beam is divided into two replicas by using a beamsplitter, and the second beam is delayed by a conventional optical delay stage [11] in respect of the first one. This delay time between pulses was previously described as the population time t_2. Both beams are later focused by a spherical mirror into a diffraction grating which produces four identical pulse replicas placed in the four corners of a square. This spatial geometry of the four beams is known as BOXCARS geometry, and it can be found in Figure 2c.

Another spherical mirror reflects on and then focuses all the beams in the sample plane. Later, the first two laser beams are simultaneously and mechanically chopped with rotating disk choppers (numbers 1 and 2 on Figure 3). The four pulses replicas are temporary split into two pairs: the pair formed by pulses 1 and 2, which come from the first beam; and pulses 3 and 4 (LO), which come from the delayed second beam. It is necessary to delay pulses 1 and 2 with interferometric accuracy, setting up the coherence time t_1. The pathways of pulses 1 and 2 include two pairs of wedges, one in each pulse. One wedge in the pair is moved in and out, resulting in a delay of either more or less dispersion for an accurate t_1 scanning.
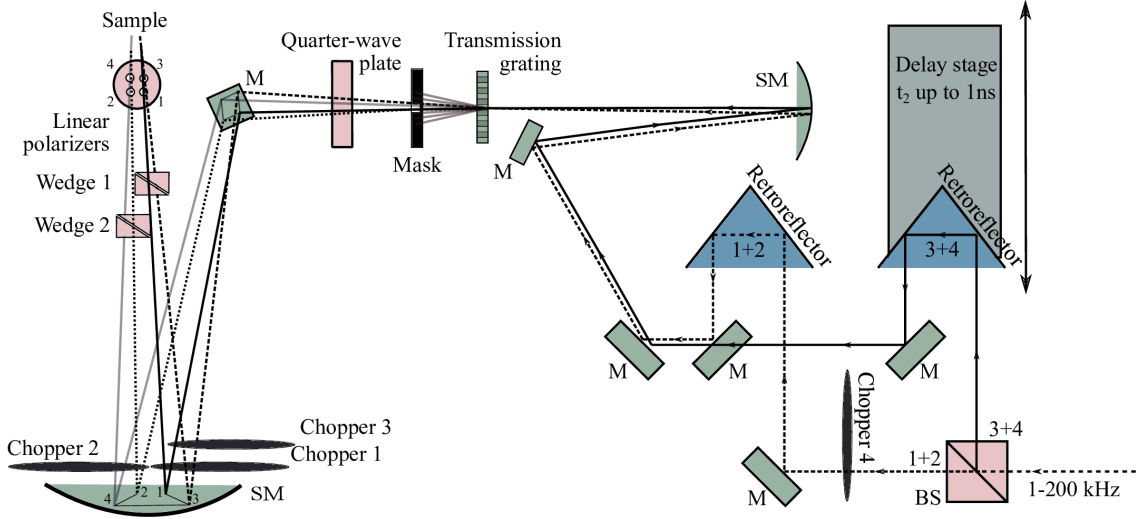
Figure 3: 2D BOX including the pathway of the laser beams schematically represented. The input laser can be found on the bottom-right part of the picture, while the output is found at the top-left part, where it interacts with the sample.

For polarization control, a quarter waveplate is used to generate circularly polarized light. Four wire grid polarizers in each of the beams set the proper linear polarization for each experiment [11]. As explained before, the interaction of the first three pulses induces a third-order non-linear polarization in the sample, which then emits an electric field that interferes with the LO. The resulting spectral interferogram is recorded by a CCD camera. Finally, one exclusive feature employed in the set up is the double lock-in detection system, implemented by opto-mechanical modulation of beams 1 and 2 [11]. With it, it is possible to suppress a larger amount of scatter from the sample.

4.3   Theoretical basis of non-linear spectroscopy

2DES measures the 3rd order non-linear polarization of a system. A full in-depth theory explanation is described elsewhere in detail [10, 12]. Although giving this description is not the object of this work, some minimal theoretical background is needed for understanding the signals observed in 2DES experiments. Therefore, this section will quickly explore the most important elements when it comes to describe non-linear spectroscopy experiments.

A quantum mechanical state of a single molecule that can be described by a single wavefunction is called a "pure state". Here, as the goal is to work with a perturbed reference system, it is very convenient to use the interaction picture to describe the system. Then, it can be defined the total Hamiltonian as the sum of the time-independent molecular Hamiltonian $\hat{H}_0$ and the *interaction* with a time-dependent electric field $\hat{W}(t)$ [10]:

$$\hat{H}(t) = \hat{H}_0 + \hat{W}(t), \tag{1}$$

with:

$$\hat{W}(t) = -\hat{\mu}E(t), \tag{2}$$

where the electric field, $E(t)$:

$$E(t) = 2E_0(t)\cos(\omega t + \vec{k} \cdot \vec{r}) = E_0(t)\left(e^{-i\omega t + i\vec{k}\cdot\vec{r}} + e^{+i\omega t - i\vec{k}\cdot\vec{r}}\right), \tag{3}$$

7

where $\hat{\mu}$ is the transition dipole moment of the quantum system, ω the optical frequency of the laser field, κ a wave vector and r is a space vector. The pure state described by the molecular wavefunction evolves following the Schrödinger's time-dependent equation:

$$\frac{d}{dt}|\psi(t)\rangle = -\frac{i}{\hbar}H(t)|\psi(t)\rangle. \tag{4}$$

That can be expanded in an eigenstate basis of the molecular Hamiltonian:

$$|\psi(t)\rangle = \sum_n c_n(t)|n\rangle, \tag{5}$$

where c_n are the probability amplitudes. Then, the expectation value of the physical property described by the operator $\hat{O}$ for a pure state described as in equation 5 is:

$$\langle\psi(t)|\hat{O}|\psi(t)\rangle = \sum_{nm} \rho_{nm}(t)O_{mn} = Tr(\hat{\rho}(t)\hat{O}) = \langle\hat{\rho}(t)\hat{O}\rangle, \tag{6}$$

where Tr is the trace over the matrix, being introduced in the description of a density matrix as follows:

$$\rho_{nm} = c_n c_m^*. \tag{7}$$

This can be also introduced in Schrodinger's equation 4 obtaining, after some calculus, the called "Liouville von Neumann" equation:

$$\frac{d}{dt}\rho = -\frac{i}{\hbar}(\hat{H}\rho - \rho\hat{H}) = -\frac{i}{\hbar}[\hat{H}, \rho], \tag{8}$$

where [,] is a commutator, and the Hamiltonian operator is applied at both left and right sides of the density matrix. As long as the described state is a pure state, both equations 4 and 8 are equivalent:

$$\frac{d}{dt}|\psi\rangle = -\frac{i}{\hbar}H|\psi\rangle \quad \Leftrightarrow \quad \frac{d}{dt}\rho = -\frac{i}{\hbar}[H, \rho]. \tag{9}$$

However, this is not the case in common experimental situations, statistical ensembles of molecules are found rather than pure states. It is not possible to write a wavefunction of a statistical average, but it is possible to do that with a density matrix as follows:

$$\rho(t) = \sum_i p_i |\psi_i\rangle \langle\psi_i|, \tag{10}$$

where p_i is the possibility of the system being in ψ_i state, $p_i > 0$ and $\sum_i p_i = 1$.

The density matrix of a statistical ensemble is defined, and including it in the Liouville von Neumann equation leads to one additional term, which includes dephasing:

$$\dot{\rho}_{nm} = -\frac{i}{\hbar}\left[\hat{H}_0, \rho\right]_{nm} - \frac{i}{\hbar}\left[\hat{W}_0, \rho\right]_{nm} - \rho_{nm}/T_2. \tag{11}$$

It is possible to solve the equation iteratively by integration and express the result as a series of $\rho^{(n)}$, where (n) is the order in powers of $W(t)$. In 2DES experiments, the signals are proportional to the third order polarization of the sample, and then we have:

$$P^{(3)}(t) = \int_0^\infty dt_3 \int_0^\infty dt_2 \int_0^\infty dt_1 E_3(t - t_3) E_2(t - t_3 - t_2) \cdot E_1(t - t_3 - t_2 - t_1) R^{(3)}(t_3, t_2, t_1), \tag{12}$$

where $R^{(3)}(t_3, t_2, t_1)$ is one 3rd order non-linear response:

$$R^{(3)}(t_3, t_2, t_1) = -\left(-\frac{i}{\hbar}\right)^3 \langle\hat{\mu}(t_3 + t_2 + t_1)[\hat{\mu}(t_2 + t_1), [\hat{\mu}(t_1), [\hat{\mu}(0), \rho(-\infty)]]]\rangle. \tag{13}$$

In the response function, $\rho(-\infty)$ is the equilibrium density matrix before the system interacts with the light fields. The response function is single sided only when $R^{(3)}(t_3, t_2, t_1) \neq 0$, or when $t_1 \geq 0$, $t_2 \geq 0$ and $t_3 \geq 0$, which means that the system only emits the electric field after the three interactions with the laser pulses [10]. This is due to the fact that after the three interactions, the system ends up in the optical coherence state (presence of non-zero off-diagonal values in the density matrix), and then is forced to emit an electric field at time $t_3 + t_2 + t_1$.

There exists a large number of possible interaction sequences, or *pathways*, given by equation 12, due to the interaction of the three electric fields with the system. As it can be observed in these equations, each interaction causes the density matrix to be perturbed through the transition dipole moment operator [11]. As the response function involves three commutators, the dipole moment operator can eventually act on both sides of the density matrix. These complex pathways can be represented by the so-called "double-sided Feynman diagrams".

However, it is not necessary to take into account this large amount of possible pathways. Some of them are not physically possible, and some others can be eliminated by experimental design. As it can be observed in Figure 2, phase-matching is fundamental for this purpose. In the known as BOXCARS geometry, only signals where the phase-matching produces an overlap between the emitted field and the LO will be detected. This leads to the detection of two main pathways of interaction, rephasing ($k_s = -k_1 + k_2 + k_3$) and non-rephasing ($k_s = k_1 - k_2 + k_3$) signals. This fact, combined with the known pulse-ordering and rotating wave approximation [10], will allow only four types of pathways in each of the phase-matching directions. Without considering the double quantum coherence pathways, these pathways are represented in Figure 4 with the double-sided Feynman diagrams for a three levels system (ground state $|g\rangle$, excited state $|e\rangle$ and superior excite state $|f\rangle$).
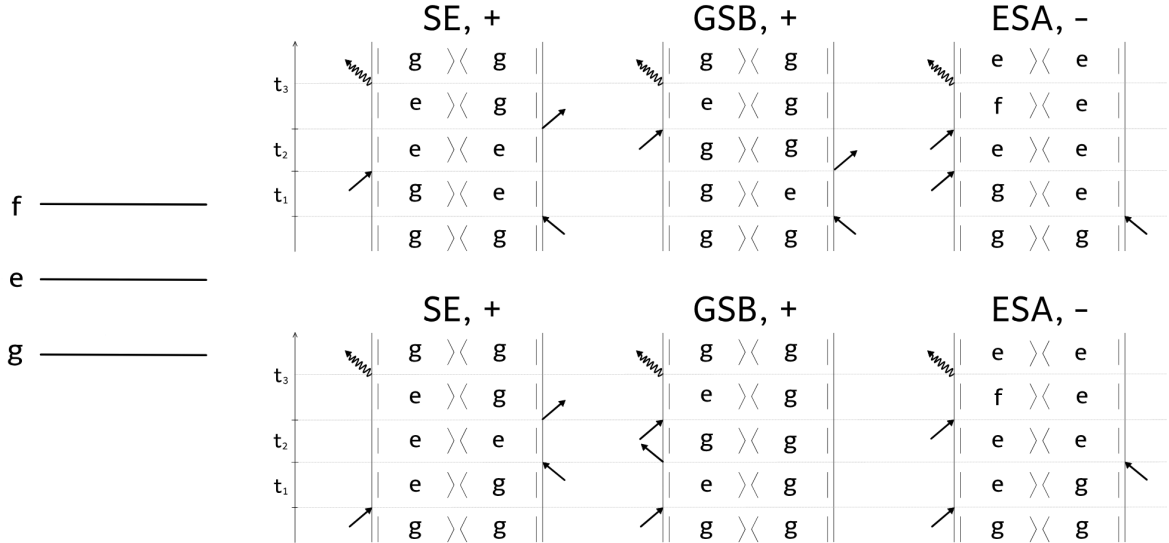

Figure 4: Double-sided Feynman diagrams for a three energy level system when it interacts with three laser pulses and it is forced to emit an electric field after the induced third order non-linear polarization. Top row corresponds to rephasing signals (first interaction from the right) and bottom row corresponds to non-rephasing signals (first interaction from the left). Stimulated emission (SE) signal is related to response functions R_1 and R_4; ground state bleaching (GSB), to R_2 and R_5; and excited state absorption (ESA), to R_3 and R_6. Double-quantum coherences diagrams are excluded from the figure. Rules who are followed to the construction of diagrams are explained below.

In Figure 4, the top row of diagrams correspond to rephasing signals; and the bottom row, to non-rephasing signals. Their response functions are numerated from left to right and top to bottom, as follows:

$$R_1 = i \langle \mu_3 \mu_1 \rho(-\infty) \mu_0 \mu_2 \rangle, \tag{14}$$

$$R_2 = i \langle \mu_3 \mu_2 \rho(-\infty) \mu_0 \mu_1 \rangle, \tag{15}$$

$$R_3 = -i \langle \mu_3 \mu_2 \mu_1 \rho(-\infty) \mu_0 \rangle, \tag{16}$$

$$R_4 = i \langle \mu_3 \mu_0 \rho(-\infty) \mu_1 \mu_2 \rangle, \tag{17}$$

$$R_5 = i \langle \mu_3 \mu_2 \mu_1 \mu_0 \rho(-\infty) \rangle, \tag{18}$$

$$R_6 = -i \langle \mu_3 \mu_2 \mu_0 \rho(-\infty) \mu_1 \rangle. \tag{19}$$

The rules for drawing and understanding double-sided Feynman diagrams are well summarized elsewhere [10], but they are listed bellow to make the work easier to read and follow:

1. The density matrix of the system can be found on the central part of the diagram. The Feynman diagram tracks its temporal evolution from bottom to top.

2. Interactions with the light field are represented by arrows. The system begins always in the $|g\rangle\langle g|$ state, and after the three interactions with pulses, it is forced to emit. Interactions with laser pulses and the final emission are represented with straight arrows or curved arrows respectively. This final emission is only plotted from the *ket* (left), because the corresponding diagrams with the emission from the *bra* (right) are just the conjugate complex and do not carry any additional information.

3. The directions where the arrows point determine whether the field of the pulse is $e^{-i\omega t + i\kappa r + i\phi}$ (pointing left) or $e^{+i\omega t - i\kappa r - i\phi}$ (pointing right) when interacting with the system. The emitted light, represented in the last interaction, has a frequency and wavevector that is the sum of the input frequencies and wavevectors.

4. Interactions whose arrows point towards the density matrix excite the system, promoting the *ket* or *bra* to higher states; while those that point outwards the density matrix represent the de-excitation of the system. Therefore, the last interaction is always pointing out of the density matrix.

5. The frequency of the first and the last interactions determines the position of the signal in the 2D spectrum along ω_1 and ω_3 respectively.

6. The last interaction must end in a population state. In linear spectroscopy, this will be the ground state $|0\rangle\langle 0|$, but in nonlinear spectroscopy, this can also be higher excited states like $|g'\rangle\langle g'|$ or $|e'_1\rangle\langle e'_1|$.

4.4 2DES signals

Generally speaking, a 2D spectrum is a correlation spectrum between excitation and detection frequencies for a fixed t_2. Diagonal peaks are related to the linear absorption spectrum of the system, and cross-peaks signify the coupling between the system states and can track the energy transfer. Peaks, with their corresponding intensities, are constructed with the signals whose pathways are shown in figures 4 and 5. Therefore, we have two main ways to categorize the contributing signals: either with the rephasing or non-rephasing character or depending on which of the three physical types of signals (SE, GSB or ESA) they are.

Further comprehension on how rephasing and non-rephasing signals are obtained is necessary at this point. As it can be observed on the Feynman diagrams in Figure 4, the only difference is the change of position of the order of the first two sample-pulses interactions. In the experimental set up, one pulse has a
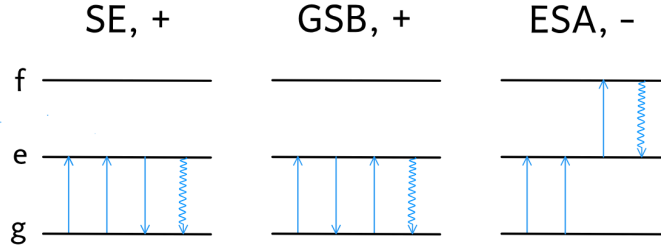
Figure 5: Representation of the possible pathways shown in Figure 4. Straight lines represent interactions with a laser pulse and curve lines represent the final emission of the electric field. Lines are drawn in temporal order from left to right.

positive phase, $+\kappa$; therefore, in the Feynman diagrams is always pointing left, with an electric field having a factor $e^{-i\omega t + i\kappa r + i\phi}$. The other pulse has a negative phase, $-\kappa_2$; therefore, in the Feynman diagrams is always pointing right, with an electric field factor $e^{+i\omega t - i\kappa r - i\phi}$. By manipulating the order in which these pulses interact with the sample, both rephasing and non-rephasing signals can be obtained: rephasing, if the pulse with negative phase arrives first; and non-rephasing, if the pulse with positive phase arrives first.

On the one hand, the rephasing signal is characterized by an all-inclusive time-dependent phase factor of $e^{-i\omega t_1 + i\omega t_3}$, evolution that corresponds to counter-propagating phase factors during t_1 and t_3. This is why it is called "rephasing signal", because the ensemble dephasing acquired during t_1 is turned around during t_3, resulting in the rephasing of the individual systems factors [11]. The optical phenomena of photon echo is caused by this, where the signals from molecules with different transition frequencies behave at time $t_1 = t_3$ as if they all had the same corresponding phases equal to zero.

On the other hand, the non-rephasing signal is characterized by an all-inclusive time-dependent phase factor of $e^{-i\omega t_1 - i\omega t_3}$. It does not have this counter-propagating phase factor and, therefore, it does not have the rephasing character.

Continuing with the explanation of the three physical types of signals, it is convenient to follow the analogy between pump-probe and 2DES experiments introduced in the section 4.1. In 2DES, the first two pulses can be understood as "pump" pulses, because they prepare the density matrix that then evolves freely during the population time t_2. Therefore, these three signals can be described as follows:

- Stimulated emission (SE) signals are described by the response functions R_1 and R_4. They evolve in the excited state $|e\rangle\langle e|$ during t_2, which eventually is probed to the ground state $|g\rangle\langle g|$. The intensity of this signal is by convention plotted as positive intensity.

- Ground state bleaching (GSB) signals are described by the response functions R_2 and R_5. They evolve in the ground state $|g\rangle\langle g|$ during t_2 and, eventually, end up also in the ground state $|g\rangle\langle g|$. The intensity of this signal is also plotted as positive intensity.

- Excited state absorption (ESA) signals are described by the response functions R_3 and R_6. They evolve, as SE response functions, in the excited state $|e\rangle\langle e|$ during t_2, but the last two interactions probe the absorption to higher energy states, ending up in the excited state $|e\rangle\langle e|$ after t_3. Therefore, the overall sign of these signals is negative, opposite from the other two interactions.

However, the pulse sequence applied in 2DES can create coherences, which are superpositions of the energy eigenstates of the sample. The coherences evolve in the population time t_2 with a phase factor of $e^{\pm i\omega_2 t_2}$, being ω_2 the frequency difference between the two states implicated on the superposition. The origin and description of coherences rely on physical models which describe the interaction between light-matter and sample-enviroment [13]; and the debate about the meaning and implications of these coherences for the

11

biological function of the same, or if there is any, is still going on [14, 15]. The next section will go deeper into all of these topics, as the way to demonstrate the vibronic mixing in Chl a, the main topic of this work, relies on the interpretation of the observed coherences [3].

4.5 Quantum coherences and quantum beats in 2DES measurements

4.5.1 Coherences and oscillation maps

Coherences are not a unique feature of the quantum systems, they are also present in classical systems. Some examples of classical coherences can be found on different phenomena, like the iridescence of insect wings or soap bubbles [16], the motion of a pendulum [17], the speckle observed in scattered laser light [18] or the propagation of electromagnetic waves [19]. While the classical coherences rely on the linear addition of light's electromagnetic fields, the quantum coherences are consequence of the sum of amplitudes in a quantum superposition of states [14]. In both cases, the fixed phase relationship between the fields of the ensemble is necessary to produce the constructive interference, which will persist in the space and/or time [14].

The technical way to define coherences is as the off-diagonal elements in any density matrix [14, 15]. However, the physical interpretation of these off-diagonal elements rely on the choice of the employed basis [20], for example, the site or excitonic basis. Nevertheless, in a recent work about the quantum nature of biology [15], the concept of coherence is reviewed, finding the definition of coherence as "*the off-diagonal elements in the density matrix in the basis of system eigenstates*" more useful. With this, coherences can be understood as the degree of linear superposition of quantum eigenstates of a system, which can be induced by light. When the source employed for generating these superpositions consists of short laser pulses, the coherences are non-stationary and, therefore, they evolve in time and can be detected as oscillating signals. Their frequency is the difference between the eigenstates involved in the superposition. In our experiments, the quantum coherences described as before manifest as oscillations, and they are called "quantum beats". The information that can be extracted from quantum beats is useful, as it is related to fundamental properties of the system itself and its interaction with the environment.
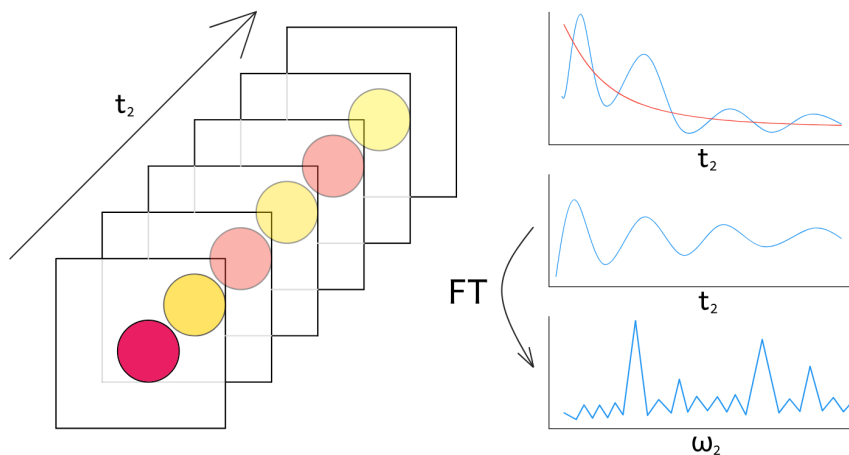

Figure 6: Schematic representation of quantum beats. Left: the intensity of some points of the 2D spectra is oscillating during the population time t_2, and it can be extracted. Top right: the intensity of the point oscillates, but also have the inner dynamics of the energy transfer present at that point. Multiexponential fit (red) is needed to extract the pure oscillations from the present kinetics. Center right: intensity of the residuals from the previous fit in population time. Bottom right: a Fourier transform is performed from the previous residuals to obtain the frequency of the oscillations, ω_2.
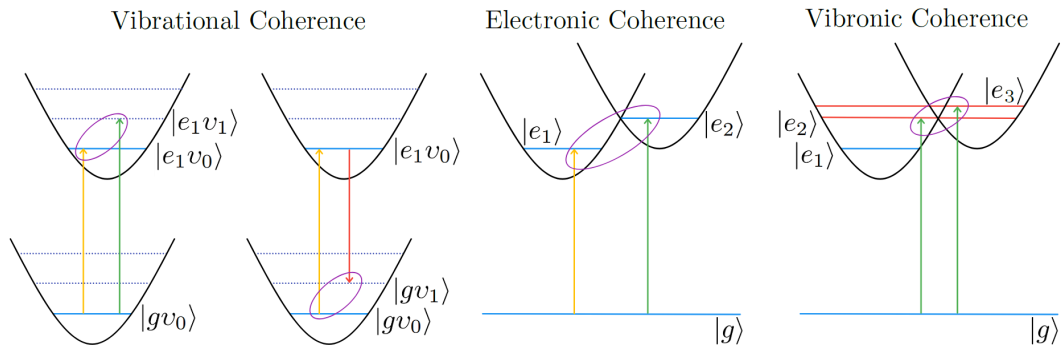
Figure 7: Schematic representation of the superposition of states involved in the different types of coherences. As quantum beats are observed during population time, the superposition of states is created after two interaction with laser pulses and, therefore two transitions are shown in each case. All the possible pathways for creating coherences will be shown later. In the case of vibrational coherences, they can be generated in the excited electronic state (first from the left) or in the ground state (second from the left). Color code for transitions is explained in Figure 8.

One important fact about coherences is that they evolve in time with certain decay rate that can be measured. This decay is called "dephasing", and it provides information about coupling between system and environment [14]. It is caused by the different local environments that surround the pigments, which cause that the members of the ensemble acquire phase at different rates, making the amplitude of the generated quantum beats weaker. The crucial process that causes dephasing is known as "decoherence", which leads to the loss of quantum coherences in every system that is not perfectly decoupled from its environment [21]. Dephasing of different types of coherences is caused by different dephasing factors. These, therefore, decay at different rates [14]. Electronic decoherence usually happens within 10-100fs [22], and vibrational decoherence in much larger times (1ps [23]). In the case of vibronic decoherence, an intermediate timescale between previous cases is found [24]. Therefore, the study of these lifetimes might be a way to characterize and understand the coherences observed in a 2DES experiment.

As it has been introduced before, there are different types of quantum coherences depending on which states are involved in the superposition. A schematic visualization of the models can be found in Figure 7, which are shortly described, as follows:

- Electronic coherence. It is constructed when the superposition involves electronic states.

- Vibrational coherence. It is caused by the superposition of vibrational states, either in the excited or in the ground electronic state.

- Vibronic coherence. It happens when excited vibronic states are involved, and implies vibronic coupling that mixes both electronic and vibrational states.

In 2DES experiments, the superposition of eigenstates is created by the first two pulses and, therefore, the coherences evolve during the population time t_2. Because of this, one approach to quantum beats can be made with the so-called "3D Electronic Spectroscopy" [25, 26]. Another Fourier transform is performed here along t_2, obtaining a spectra with a signal of the type $S(\omega_1, \omega_2, \omega_3)$ and creating a cube map that can be represented in three dimensions. The slices that can be made from this spectra can generate another type of 2D map in function of both ω_1 and ω_3 but, in this case, for a fixed ω_2 instead a fixed t_2. These maps, in the proper ω_2 frequency, provide a lot of useful information about the oscillations. The characteristics of these "beating maps" will be discussed later.

Schematic in Figure 6 is given with the aim to facilitate understanding of quantum beats. In certain parts of the 2D spectra (like cross peaks), these quantum beats are observed. They make it possible to extract the signal amplitudes (and phases) as a function of the population time. This signal reveals both coherent and
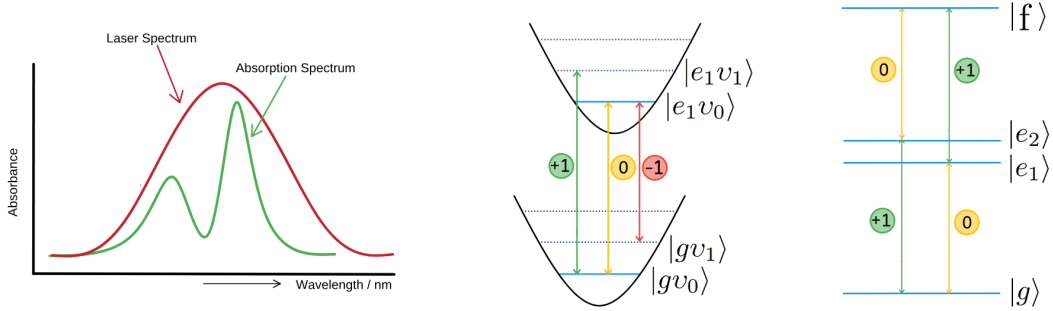
Figure 8: Left: linear absorption spectrum corresponding to a couple of physical models of the system which can feature coherences. They appear together with a broad laser spectrum that covers it. Both models have the same spectra but exhibit distinct internal coherence dynamics [13]. Center: energy levels of a displaced oscillator (DO), physical model which describes vibrational coherences. Right: energy levels of an electronic dimer (ED), physical model which is related to electronic coherences. In the model a color and numerical code is used, which will be employed in the rest of the work to describe the energy of transitions.

incoherent dynamics of the system. The coherent dynamics are observed in the oscillatory character; and the incoherent dynamics in the multi-exponential decay. In Figure 6, the signal amplitude is shown in blue and the exponential fit in red. The residuals of the fit (subtractions of the fit value from signal amplitude) have only the coherent (oscillatory) character of the signal, and performing a FFT (fast Fourier transform) over it can reveal the frequencies of the coherences.

Another relevant factor when studying coherences is the fact that the beating frequency, ω_2, which has the same energy as the energy difference between states involved in the superposition, can have a similar energy order for vibrational, electronic or vibronic coherences; therefore, beating frequency is not a good indicator for categorizing them. The problem about how to distinguish the electronic or vibrational origin of the beats in 2DES experiments can be addressed considering two physical model systems which can have similar absorption spectra but exhibit different internal coherent dynamics [13]. These models are schematically represented in Figure 8.

They represent the simplest approach to systems that have either vibrational (DO) or electronic/vibronic (ED) coherences. Both of them might lead to practically indistinguishable 2D spectra with presence of quantum beats. However, as their inner energy structure is rather different, the contributions that they make to the oscillation maps is also different [13]. Then, the study of quantum beats is not going to be made from the FFT performed on the t_2 axis at a single point of the 2D spectra, but from the simultaneous analysis of all the beats present in the full 2D map [15].

The oscillatory contributions that both models feature in the beating maps can be found in Figure 9 [13]. DO model is considered here with only two lowest vibrational sub-states. As it can be observed, DO system contributes with 8 rephasing and 8 non-rephasing signals to the total beating maps, and ED system contributes with 4 rephasing and 4 non-rephasing signals. The contributions to the oscillatory maps are grouped in 6 key positions in the DO model and in 4 key positions in the ED model. The presence of signals in the bottom row position is therefore an indicator that allows to differentiate the origin of the signals.

However, the maps constructed with all the oscillations are rather complex to read and understand, this is why some simplifications would be desirable. First of all, separating the contributions in their rephasing and non-rephasing parts allows to some simplification. As the information contained in both parts separately is basically the same, for further analysis only rephasing oscillations are considered. Second, as the amplitude and phase of the signal is measured, it can be recast in the complex plain with its real and imaginary parts. Signals that evolve with the opposite phase can be separated and, therefore, allow construction of beating maps with positive and negative frequencies. To achieve that, the oscillation maps have to be constructed by performing a complex Fourier transform instead of a real Fourier transform [15].
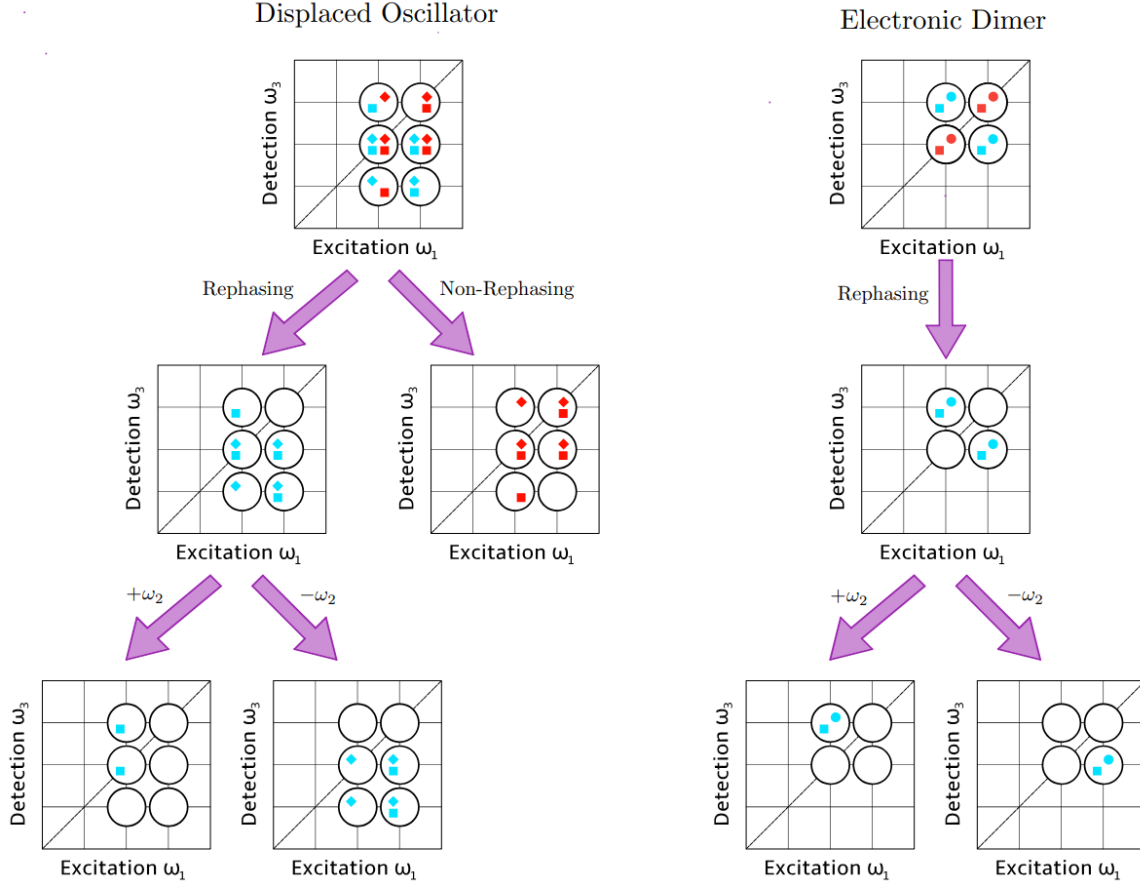
14

Figure 9: Schematic representation of oscillatory contributions of DO model system and ED model system to the beating maps. Color code: blue for rephasing, red for non-rephasing signals. Geometric code: squares for SE, diamonds for GSB, circles for ESA. Energy increases to the top (y-axis) and to the right (x-axis). Displaced oscillator contributions are separated in rephasing and non-rephasing. Furthermore, thanks to the complex FFT performed along t_2, it is possible to obtain positive and negative frequencies and, therefore, achieve more simplification of the beating maps. Only separation of rephasing oscillations of the ED system are shown in the figure.

4.5.2   Coherence pathways

All the coherence pathways for the DO model system and the ED model system are collected in figures 10 and 11 respectively. They are represented with double-sided Feynman diagrams following the rules described in previous sections. In the diagrams, ground state is represented as $|g\rangle$ and excited state as $|e\rangle$, with a numerical subscript which indicates the vibrational level occupied for the DO model or the electronic excited state occupied for the ED model (see fig. 8). Light-system interactions have now a color code related to the energy of the transition, and it can be found on Figure 8. As the coherences appear and evolve during t_2, the state of the system is highlighted after the second light interaction. Thus, it is possible to observe the superposition of states that generates the beatings. Those marked in blue color are related to coherences with positive phase, evolving with $+\omega_2$ in the complex analysis; while the ones marked in red color are related to coherences with negative phase, evolving with $-\omega_2$ frequency. Beating maps from the experiments done with Chl a have been chosen to serve as examples of the expected patterns. However, as it will be discussed later, it is not possible to prove the vibrational or electronic/vibronic character of the $\omega_2 = \pm 600 cm^{-1}$ beating maps.

SE, +

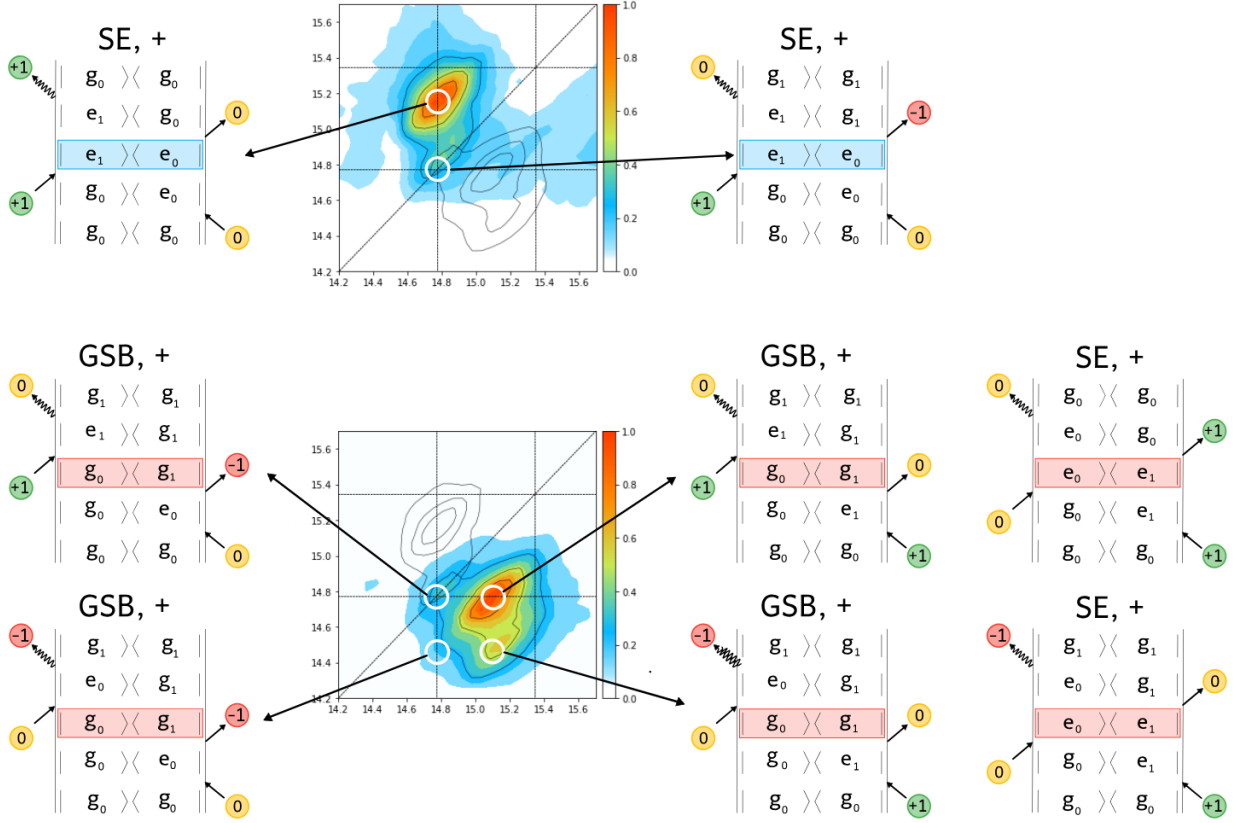SE, +

GSB, +

GSB, +

SE, +

GSB, +

SE, +

GSB, +

Figure 10: Oscillation maps of Chl a extracted from the 2DES (AP) experiment. Complex FT was performed, separating contributions from $\pm\omega_2$ pathways. Top map corresponds to $\omega_2 = +340 cm^{-1}$, and bottom map to $\omega_2 = -340 cm^{-1}$. Every map is normalized to their maximum amplitude value point. Black contour lines for the complex opposite beating map have been drawn in every map.

4.6 Polarization-control 2DES in the study of quantum beats

Polarization control is a valuable tool in 2DES experiments, where it is possible to set up specific individual polarizations of the four interactions with the field. The control of different linear polarization helps to suppress or enhance different signals that correspond to different interaction pathways. In contrast with PP experiments, 2DES has four pulse interactions available instead of two, which allows for a larger variety of polarization sequences [11]. The theory of signal selection is based on the orientational mean for all molecules or molecular systems, typically anisotropic. This averaging gives rise to multiple orientation factors for different pathways that can be improved, suppressed or omitted.

Considering the polarization of the four pulses, a, b, c, d, and the orientation of transition dipole moments that interact with any response signals, α, β, γ, δ, the orientational factor of a particular signal is $\Omega = \langle a_\alpha b_\beta c_\gamma d_\delta \rangle$. It can be expressed as follows [27], [28]:

$$
\begin{aligned}
\langle a_\alpha b_\beta c_\gamma d_\delta \rangle = \frac{1}{30} \{ &\langle \cos\theta_{\alpha\beta} \cos\theta_{\gamma\delta} \rangle \left(4\cos\theta_{ab}\cos\theta_{cd} - \cos\theta_{ac}\cos\theta_{bd} - \cos\theta_{ad}\cos\theta_{bc} \right) \\
+ &\langle \cos\theta_{\alpha\gamma} \cos\theta_{\beta\delta} \rangle \left(4\cos\theta_{ac}\cos\theta_{bd} - \cos\theta_{ab}\cos\theta_{cd} - \cos\theta_{ad}\cos\theta_{bc} \right) \\
+ &\langle \cos\theta_{\alpha\delta} \cos\theta_{\beta\gamma} \rangle \left(4\cos\theta_{ad}\cos\theta_{bc} - \cos\theta_{ab}\cos\theta_{cd} - \cos\theta_{ac}\cos\theta_{bd} \right) \}
\end{aligned}
\tag{20}
$$

In the previous equation, θ_{ij} are the angles between any of the corresponding vector directions, and the $\langle\,\rangle$ are used for the orientational averaging. The total orientational factor determines the amplitude of each contribution to the 2D spectrum. By setting up some specific polarization sequences in the experiments, the
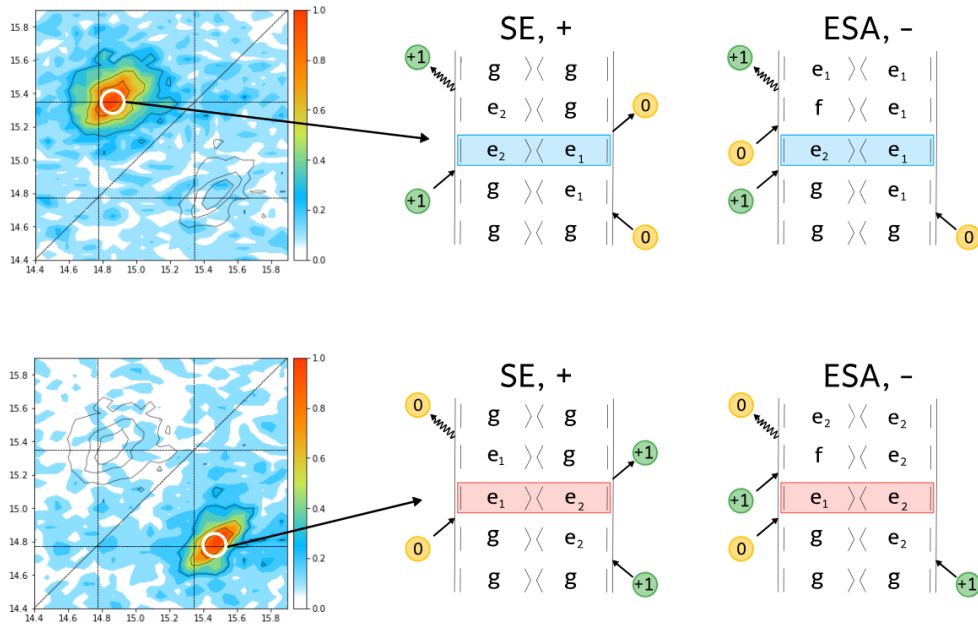
Figure 11: Oscillation maps of Chl a extracted from the 2DES (DC) experiment. Complex FT was performed, separating contributions from $\pm\omega_2$ pathways. Top map corresponds to $\omega_2 = +600cm^{-1}$, and bottom map to $\omega_2 = -600cm^{-1}$. Every map is normalized to their maximum amplitude value point. Black contour lines for the complex opposite beating map have been drawn in every map.

orientational factor can be equal to zero for some signals; therefore, they can be completely suppressed.

To understand how polarization control affects different signals, it is useful to consider a few theoretical pathway examples and study their relationship with the orientational factor. For example, the system might be composed by two weakly coupled transition dipoles, named as 1 and 2. The light pulses can interact with the system through their transition dipoles, considering only the following sequences: (1111), (1122), (1212) and (1221), and those ones that can be obtained by exchanging 1s to 2s and vice versa.

If the four interactions affect the same transition dipole, (1111) or (2222), the result corresponds to diagonal peaks, including both GSB and SE contributions and the vibrational coherences [13]. (1122) then corresponds to correlation cross-peaks and energy transfer. Finally, (1212) and (1221) are related to coherence signals, which first need two interactions to have different frequencies and different transition dipole moment orientations. Some of the most common polarization sequences employed in 2DES experiments are:

- All Parallel (AP), $(0^o\, 0^o\, 0^o\, 0^o)$. It is the most used polarization in 2DES experiments, easy to set and results in the most intense signals. However, it does not provide any signal selectivity.

- Magic Angle Set, $(54.7^o\, 54.7^o\, 0^o\, 0^o)$. As the AP polarization, it does not provide signal selectivity, but it is better to study population dynamics, as it avoid depolarization signals.

- Cross Peak Specific (CPS), $(60^o\, -60^o\, 0^o\, 0^o)$. It removes all the (1111) type contributions; therefore, only cross-peaks would remain in the spectra [27].

- Double Crossed (DC), $(45^o\, -45^o\, 90^o\, 0^o)$. In addition to removing (1111) type contributions, it also removes the (1122) contributions, leaving only (1212) and (1221) contributions.

In experiments with double-crossed polarization control only (1212) and (1221) signals remain. Moreover, these signals only allow electronic coherences or coherences excited via vibronically coupled transitions to survive, suppressing almost completely all the population dynamics (exponential decay) and the purely vibrational coherences. Therefore, DC polarization control is a very good tool to study inter-exciton coherence and vibronic coupling in molecules and molecular systems, the latter being the aim of this project.

5   Experimental considerations and methodology

5.1   Chl a, the system under study

It has been demonstrated that chlorophyllides play a major role in photosynthesis, as they are necessary for aspects like light-harvesting, involving excitation energy transfer (via exciton-transport) or charge separation during the solar energy utilization process [1, 3]. Chl a is one of the most important exponents of this group of molecules due to several facts. It is present in all photosynthetic organisms which carry on the oxygenic photosynthesis [29]. However, these organisms can differ in the use of other accessory pigments, such us chlorophyll b [30]. Moreover, depending on the protein environment, Chl a can participate also in the primary charge separation processes and electron transporting events in the reaction centers of PS I and PS II (PS = Photosystem) [29].

Chlorophyll molecules consist of two different parts [31]: a porphyrin head and a long hydrocarbon or phytol tail, as it is observed in Figure 12b in the case of Chl a. The structure of the porphyrin is rather complex: its basic skeleton consists of four pyrrole rings bonded to each other by methine groups (see fig. 12a). Different types of substitutes can be attached to the porphyrin, which will modify the physical and chemical properties of the chlorophyll. Among them, we can find the mentioned pythol chain esterified to the IV ring in the position number 7. Finally, in the center of the porphyrin ring a cation of Mg^{2+} can be found, although in other biochemical compounds, which also contain porphyrins, this central cation might vary.
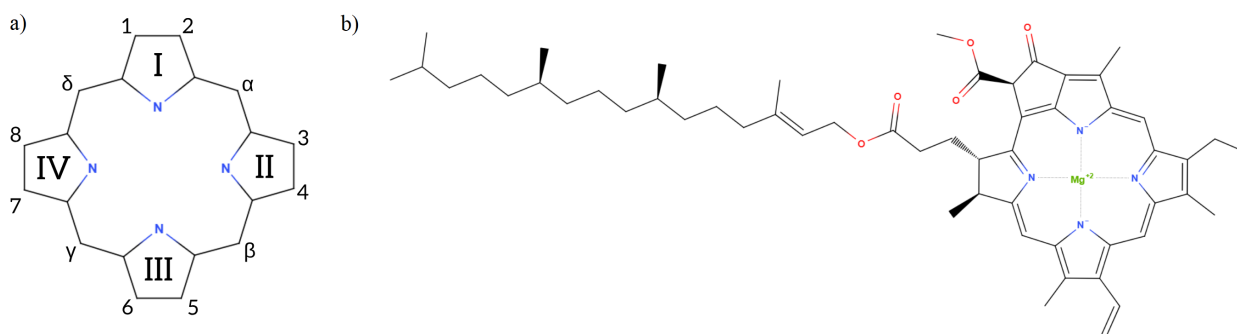

Figure 12: a) Basic porphyrin skeleton, adapted from [32]. b) Molecular structure of Chl a

The spectra of porphyrins was first interpreted by the Gouterman model [32], which was applied later to the spectra of chlorophylls in general. It is the "four-orbital model", which describes two main transitions in the visible region of the electromagnetic spectra as separate electronic transitions, known as Q_x and Q_y, with almost perpendicular mutual orientation of transition dipole moments [1]. It also labels the UV bands as B bands, having also two main transitions, the B_x and the B_y. In Figure 13a the full absorption spectrum of Chl a can be observed, with both Q and B bands visible; while in Figure 13b only the Q bands are shown. According to the arbitrary assignment of the x and y directions, which can be alternated, the highest transition in energy is the Q_x, while the other is the Q_y, at 619nm and 666nm respectively at room temperature. In fact, the Q_x band does not appear alone in the spectrum. Actually, it is overlapped with a Q_{y1} band at room temperature, which is an overtone band considered to be a vibronic replica of Q_y transition. The notation used here was described by Arvi et al. [33].

While the statements of Gouterman model point to an almost perpendicular (90°) orientation of the transition dipole moments of Q_x and Q_y, older [34, 35] and more recent [2] studies support that the real angle between the transition dipole moments is lower, slightly higher than 70°.

Talking about internal dynamics in Chl a, multiple authors explored it with different techniques, like femtosecond time-resolved stimulated emission pumping fluorescence depletion (FS-TR-SEP-FD) [36], hole-burning fluorescence line-narrowing [33], and 2DES [2, 37]. Denoting the different states of Chl a as S_0 for
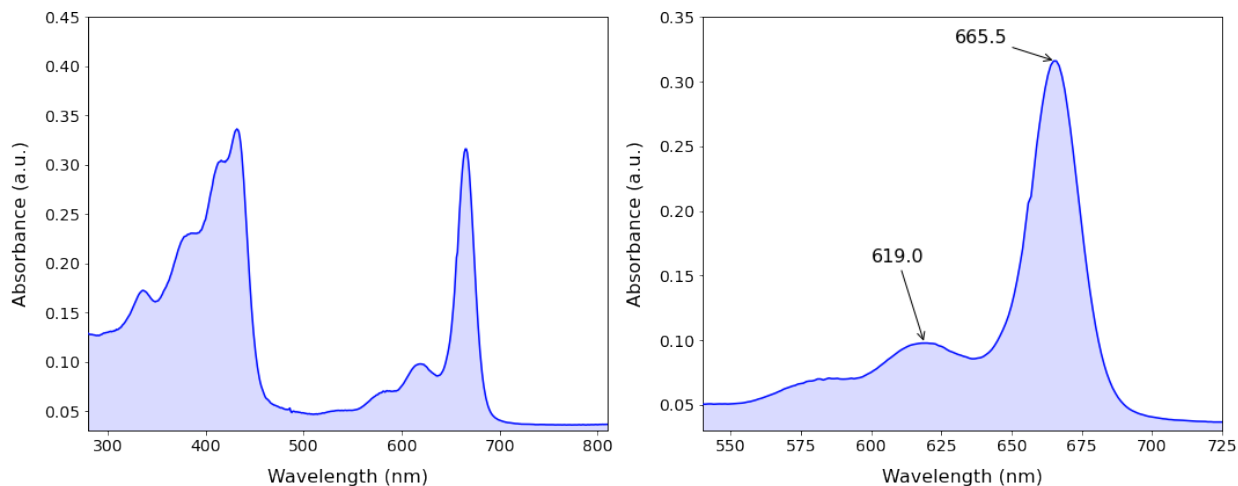
Figure 13: Absorption spectrum of Chl a at room temperature. a) Complete absorption spectrum, with both Q and B bands visible. b) Zoom in into the Q bands. At 660nm is visible the Q_y band, while at 619nm are visible both Q_x and Q_{y1} bands together; therefore, they are unresolved at room temperature.

the ground state, and S_1 and S_2 for the excited electronic states, it was found that the internal conversion within $S_2 \to S_1$ is extremely fast, and that it occurs within the first 50fs [33, 2]. This process leads to fluorescence emission of $S_1 \to S_0$ with a measured lifetime of a few nanoseconds [38]. The energy transfer between S_2 and S_1 states is much faster in Chl a than in bacteriochlorophyll a (Bchl a), where it occurs between 100-200fs [33]. This fact is correlated by the closer energy gap between Q states in chl a, $875cm^{-1}$, while in bchl a the gap is $3840cm^{-1}$. Reimers et al. relate the internal relaxation with coupling strength and resonance between the unperturbed energy gap between the Q states and the vibrational frequency [1].

The traditional assignment of Gouterman model was under debate because new techniques, like improved LD [39] and quantitative MCD [40], were key in studies that supported a different view[1]. While higher-energy component is identified as the Qx origin in the "traditional" assignment[41], the "modern" assignment selects the lower-energy one [42] as the origin. Both models fail to explain all of experimental observations of chlorophyllides and, therefore, a new global approach was needed. Based on multiple experimental data on different types of chlorophylls [1], mostly using absorption spectra and magnetic circular dichroism spectra, Reimers et al. brought forward a new theory for the energetic structure of chlorophylls. The main conclusion of the work is that "whilst most chlorophylls conform to the Gouterman model and display two independent transitions Q_x (S_2) and Q_y (S_1), strong vibronic coupling inseparably mixes these states in chlorophyll-a" [1]. Therefore, this vibronic coupling has to be taking into account when describing all the physical and chemical properties of chlorophylls, something that is also necessary for a better comprehension of the photosynthetic processes.

Vibronic coupling, also known as non-adiabatic coupling, involves the interaction between electronic and nuclear vibrational motion [43]. Born-Oppenheimer approximation fails to explain vibronic coupling because electronic and vibrational dynamics can no longer be separated, and although some corrections of the model have been proposed [43], non-adiabatic dynamics are necessary to explain the phenomena [44, 14]. Vibronic coupling leads to alteration of some properties of states involved on the mix, as the variation of the oscillator strength and the mix of their characters [3], which results in a reorientation of the transition dipole moments of those states [1, 45]. In Chl a, the expected vibronic coupling would involve an interaction between the purely electronic transition to the Q_x state, and a transition to some higher energy vibrational level of the Q_y state.

Besides being theoretically proposed, vibronic coupling might have been observed before in chlorophylls. For example, Song et al. [2] observed an evidence of vibronic coupling in Chl a in the transition dipole

moment of some of its transitions with 2DES. When assigning to the transition to Q_y state an angle of 0°, the expected transition dipole moment of transition to Q_x would be something around 70°. However, experimentally, they observed an angle of 45°. This fact was explained considering a possible mixed character of Q_x and Q_y states. That would lead to a reorientation of their transition dipole moments to an intermediate angle. Moreover, Bukartė et al. [3] performed DC polarized-control 2DES on Chl c_1; they saw some coherences that could only be excited via vibronically coupled transitions. This represents the first direct observation of this type of phenomenon.

However, Bukartė et al. worked with the Chl c_1, which is one specific type of chlorophyll found in certain photosynthetic marine algae [46]. Some issues are related to the experiments with this molecule due to its specificity. Chl c_1 is not as common, easy to obtain and to handle as Chl a, something which might raise problems with reproduction and generalization of the results. Although Chl c_1 is a better system to observe the vibronic coherences, as it will be discussed later, Chl a represents the system that might serve to demonstrate the existence of vibronic coupling as a general feature of chlorophylls.

5.2 Selection of the solvent

Based on a extensive work [33] on spectra properties of Chl a, we selected one specific solvent for it. There are many characteristics that should be taken into account when it comes to choosing a solvent. Moreover, as we are focused on the study of vibronic mixing between Q_x and Q_y transitions, some features are more important than others for this goal.

T / K	Disolvent	Coordination	Q_y / nm	Q_x / nm	$(Q_x + Q_{y1})$ / nm	ΔE / nm
295	Diethyl ether	5-CO	660.5	-	614.0	46.5
	1-propanol	5-CO	665.4	-	618.0	47.4
	2-propanol	5-CO	664.4	-	618.0	46.4
	THF	6-CO	664.5	-	628.0	36.5
	Pyridine	6-CO	671.0	-	640.0	31.0
120	Diethyl ether	5-CO	669.9	639.0	-	30.9
4.5	1-propanol	6-CO	676.8	652.0	-	24.8
	2-propanol	5-CO	669.1	627.0	-	42.1

Table 1: Some features of Chl a spectra in different solvents. Data extracted from [33].

In general, the best solvent for our experiments has to provide a well defined spectra, with the transitions traditionally denoted as Q_x and Q_y well resolved and with enough relative absorption intensity. Both transitions should be as close in energy as possible. Another factor that has to be considered is the capacity to form good optical quality glass at low temperature, something that 1-propanol and 2-propanol are able to do [33, 47].

The Table 1 shows some of these parameters. The coordination of the central Mg^{2+} ion is a relevant factor because it affects the shape of the spectra, something that can be visually appreciated in Figure 14a. At room temperature (295K), both Q_x and Q_{y1} transitions are visible in a single, broad band, while when measured at low temperatures, in some cases, they resolve either into two different bands or in a band with two shoulders. This fact can be appreciated both in Table 1 and in the Figure 14a. The way that the spectrum changes with the temperature is related to the coordination of the metal atom, which presents better structure at low temperature when the solvent shifts to a 5 coordination environment. Low temperatures also raise the OD for absorption measurements, but this factor is not taken into account because the concentration of the sample in the cuvette can be adjusted in order to achieve good OD values.

As 1-propanol and 2-propanol are well known for their quality glass at low temperatures, and the experiments are going to be performed at 77K, the analysis of the solvents is focused on them. Due to the 6-CO that 1-propanol achieves at low temperatures, its spectra structure is better defined than the one of 2-
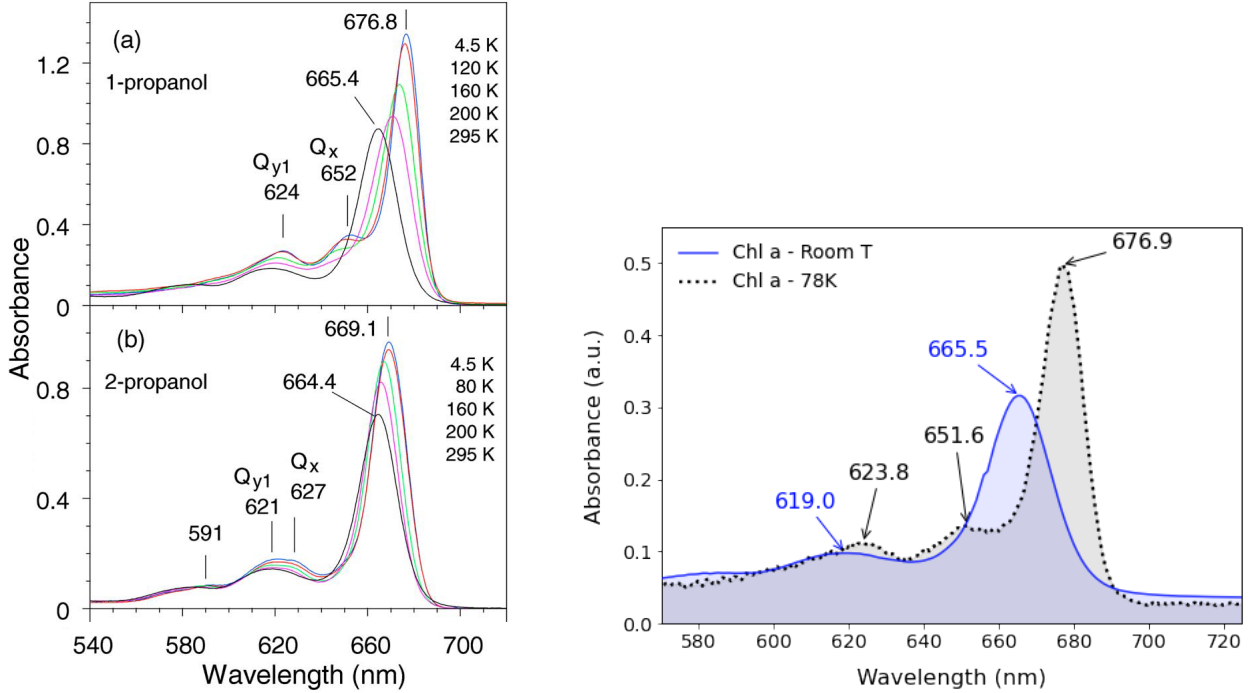
(a) Temperature dependence of Chl a absorption spectra in (a) 1-propanol and (b) 2-propanol. Vertical lines label band positions in nanometers at 4.5K. Figure taken from [33].

(b) Temperature dependence of Chl a absorption spectra in 1-propanol. Blue-solid line corresponds to room temperature spectrum and black-dashed line corresponds to 78K spectrum. Maximum peaks are pointed with arrows.

Figure 14: Temperature dependence of Chl a spectra.

propanol. In 1-propanol, Q_x and and Q_{y1} are resolved, while in 2-propanol they are present as two shoulders of the same band. Moreover, the energy difference between Q_x and Q_y transitions is lower in 1-propanol, with a value of 24.8nm vs. 42.1nm at 4.5K. These factors point to 1-propanol as the best solvent for the experiments.

5.3 Description of the experiments

A solution of Chl a in 1-propanol was prepared in a cuvette of 0.5mm thickness. Its absorption spectrum at room temperature is shown in Figure 13. The concentration corresponds to a OD of 0.30 for the Q_y transition. The cuvette was placed inside a liquid nitrogen cryostat at 78-80K under N_2 atmosphere. To perform the experiments, the cryostat was located in the "sample" position behind the "2D BOX" described in Figure 3 (top left part of the scheme). In addition to the linear polarizers before the sample, another linear polarizer was placed in the detection pathway to filter out specific signal polarization.

A total of eleven experiments have been performed with the same sample of Chl a under different conditions. Some of the conditions that varied between experiments are the focus point, temperature, polarization control and the laser spectrum.

The sample was moved between some experiments in order to avoid the "burning" of a point. Some molecules are sensible to the laser light; therefore, some of its characteristics might vary if the laser hits the sample in the same spot during long time. When looking for new spots, irregularities and cleanness of cell and cryostat have to be considered. Also, there are points in the sample that might have different concentration, more scattering than others or even cracks. These facts can vary the quality and intensity of the signal, which should always be kept optimal.
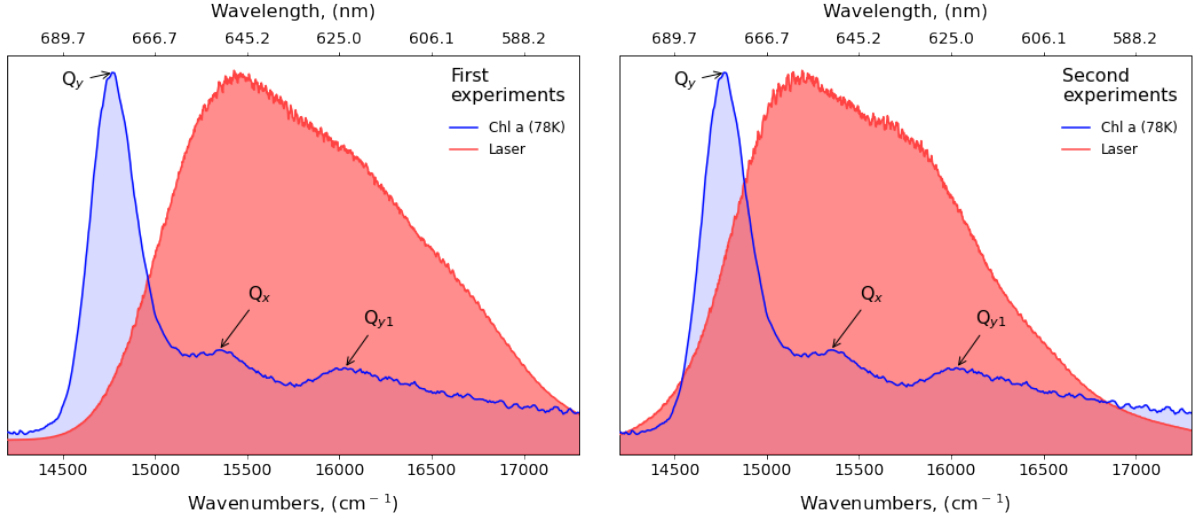
Figure 15: Spectral overlap between laser spectrum and Chl a absorption spectrum at 78K. X-axis represents frequencies (bottom) or wavelength (top), and y-axis represents intensity of either laser spectrum or optical density, in arbitrary units. Laser spectra are in red color, while chl a absorption spectra are in blue color.

Temperature was also shifted in certain occasions between experiments. According to the cryostat, with the temperature of 78K the 1-propanol glass cracked some times, so it was necessary to heat and to freeze again to obtain new good spots. In the last experiments, the temperature was set at 80K, and the low temperature glass did not crack again.

Two different polarization sequences have been used in the experiments. The first one is all parallel (AP) polarization, $(0^o\ 0^o\ 0^o\ 0^o)$, and the second one double-crossed (DC) polarization, $(45^o\ -45^o\ 90^o\ 0^o)$. The fundamental basis of this polarization set up was described in section 4.6, while the implications in the obtained results will be discussed later.

Two different laser spectrum shapes have been used in the experiments. The overlap between laser spectrum and absorption spectrum of Chl a can be found in Figure 15. In the first set of experiments, the Q_y band was severely cut in the lower energy part, while in the second set of experiments Q_y is more covered. The implications about this experimental choice will also be discussed later.

In general, experimental conditions for AP and DC experiments were kept as similar as possible. Excitation energy was $5nJ$ per pulse and all pulses were focused to a $160\ \mu m$ spot size. Population time t_2 was scanned in 10 fs time steps for different range in each experiment. Coherence time was scanned with movable fused silica wedges from -102 fs to 300 fs in steps of 1.5 fs in all the experiments.

Table 2 summarizes the different parameters used in each of the eleven experiments performed. As it can be observed, only certain values of final population times for the scans are given. In the other experiments some problems arose. Among them, we experienced problems with the stability of the LO, with the CCD camera, with the low-temperature glass stability or with the atmosphere in the cryostat. As a result, only the analysis of four experiments was done: two of them with Q_y not fully covered by laser spectrum and two of them with Q_y better covered by laser spectrum.

Pump probe experiments were also performed with AP configuration in order to phase the 2D scans. The pump probe experiments have delay times between the pump and the probe that cover all the range of 2D experiments, from -30fs to 2500fs, in different time steps (5fs until 100fs; 10fs until 300fs, 100fs until 500fs; and 500fs until 2500fs).

Number of experiment	Polarization	Spectra overlap	T / K	Date	Final t_2 time / fs
1	AP	Not fully Q_y covered	78	2020/11/13	2320
2	DC	Not fully Q_y covered	78	2020/11/15	-
3	DC	Not fully Q_y covered	78	2020/11/16	-
4	DC	Not fully Q_y covered	78	2020/11/18	-
5	DC	Not fully Q_y covered	78	2020/11/20	-
6	DC	Not fully Q_y covered	78	2020/11/24	1940
7	AP	Better Q_y covered	78	2020/11/25	-
8	AP	Better Q_y covered	80	2020/11/27	2000
9	DC	Better Q_y covered	80	2020/11/29	-
10	DC	Better Q_y covered	80	2020/11/30	-
11	DC	Better Q_y covered	80	2020/12/03	2000

Table 2: A short resume of the experimental characteristics of the experiments. Spectral overlap is given in Figure 15.

5.4 Data analysis

Different programs have been employed for the analysis of the experimental data. From data visualization to integral FFT, the distinct software was able to perform various operations. A small description of the characteristics, programming basis and functions of the software are given in the present section.

5.4.1 2D Analysis

2D Analysis [48] is the main analysis program employed after the 2DES experiments of the research group. It is written in LabVIEW, a visual programming language developed from National Instruments, which is frequently used for data acquisition, instrument control, industrial automation and data manipulation. In our case, these functions are separated in two programs: 2D Acquisition is in charge of data acquisition and instrument control, while 2D Analysis is responsible for the data extraction.

2D Analysis software can read the recorded data and work with it. Its windows settings allow to filter out specific parts of the recorded field, eliminating scattering and selecting the most important sections of the data. It also performs FFT along t_1 and t_3 axis in order to create the 2D spectra. While the recorded field might have a limited number of data points, the program is able to interpolate this data to more data points for visualization purposes. In our case, an interpolation to 200x200 data points was done in all the experiments.

Another important feature of the program is the capacity of phasing 2D experiments with PP data from the same system. The real part of the signal integrated along ω_1 and normalized to the LO electric field corresponds to the PP spectrum [11], and the analysis program can match these parts to phase the data. This is a crucial feature for the experiments because proper phasing allows clean separation of the real and imaginary parts of the response [11, 49].

Among many other features, it also can separate the 2D data into its different constituent parts and visualize them. In the complex domain, you can visualize real or imaginary parts, or both contributions at the same time. Considering the coherence time t_1, it can visualize both rephasing and non-rephasing parts, either separated or at the same time. Besides visualization, it allows the user to extract the separated data into *.txt* files to work with them in another software.

As the main goal of this project is to observe coherences excited via vibronically coupled transitions, 2D Analysis program can be used, as it can perform a real Fourier transform along t_1 to obtain a spectra of

$(\omega_1, \omega_2, \omega_3)$ and, therefore, visualize beating maps as a function of ω_2 frequencies. However, as the real FT is performed, separating the contributions in the complex domain, as shown in Figure 9, is not possible. After doing decay absorption spectra (DAS) analysis (with multi-exponential fitting), a discrete Fourier transform (DFT) can be performed in the residuals of the fit to obtain the beating ω_2 frequencies of the system. This frequencies, again, are in the real domain and not in the complex one. The desired analysis of the data involves complex FFT to obtain both positive and negative beating frequencies; therefore, further work should be done to study the signals more profoundly.
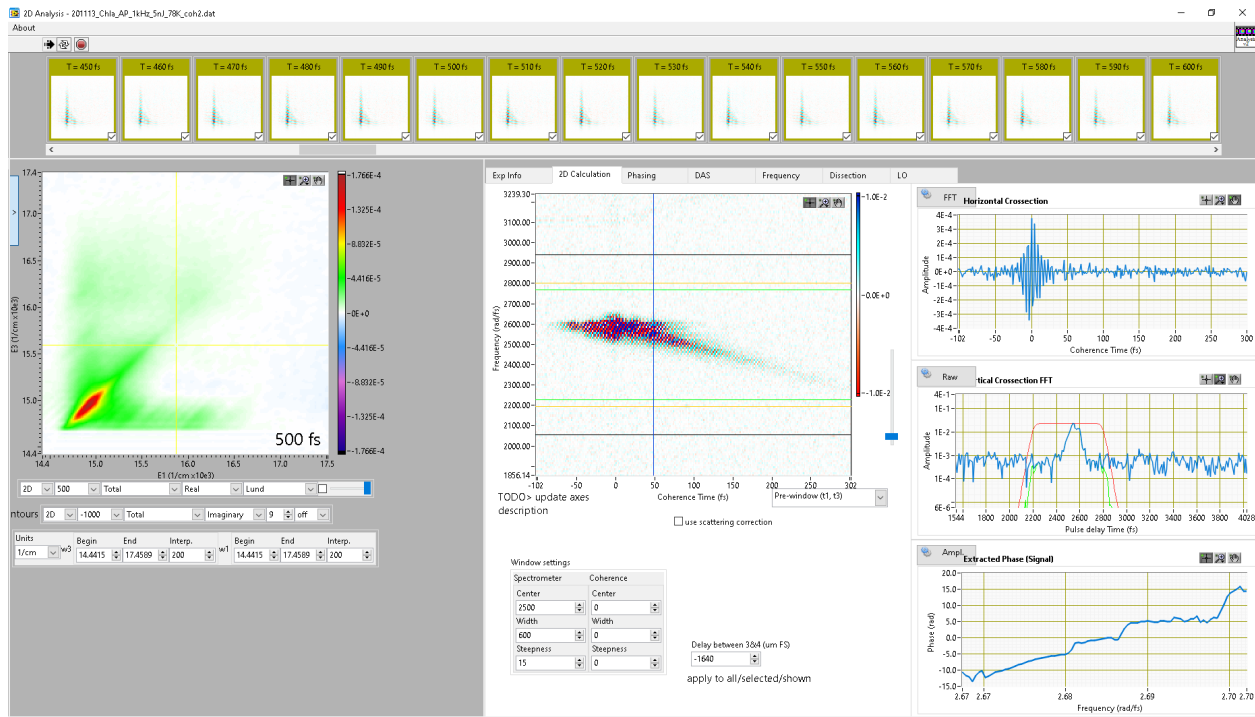
Figure 16: Interface of the 2D Analysis program. It is possible to observe some of the features of the software, such as the window settings or the 2D spectra. The hidden tabs on the right side have the options to do the phasing, the DAS analysis and the DFT along t_2 axis. In the figure, the first AP experimental data set is loaded.

5.4.2 FT Analysis

FT Analysis [50] is a program developed by David Palecek. It is written in Python 3, and consists mainly of one Jupyter Notebook's file and a set of pre-defined functions written in a Python File (.*py*). The software can perform complex FFT over the input data and, therefore, allows the user to work with both positive and negative ω_2 frequencies. The steps that the software follows to operate are the following:

1. It loads experimental data of the 2D experiment and stores it in a 3D matrix. The 3D matrix stores data in the form of $(\omega_1, t_2, \omega_3)$. Real and imaginary contributions have to be separated in different file inputs and, therefore, stored in different matrices. Only rephasing or non-rephasing data can be loaded on one go.

2. It does a multi-exponential fit of the kinetics at every single point in 2D map. In fact, it takes every (ω_1, ω_3) coordinate of the data set, performing the fit along population time t_2.

3. Software calculates the residuals of every fit and stores them in another 3D matrix $(\omega_1, t_2, \omega_3)$, where the multi-exponential dynamics are not present.

4. Program conducts a complex FFT on the residuals, returning another 3D matrix, $(\omega_1, \omega_2, \omega_3)$. This time, contrary to when employing 2D Analysis program, ω_2 values obtained are both positive and negative. At this point, the analysis can follow different directions.

   (a) First, by slicing the previous matrix on ω_2 axis, the so-called beating maps can be obtained and represented. In this case, the signal contributions can be separated on the complex domain, following the scheme showed in Figure 9.

   (b) Second, it can integrate 3D FFT matrix over the the ω_1 and ω_3 axis, so the result is a Fourier amplitude spectrum of the whole experiment. The posterior modification of the code allows the user to integrate the 3D FFT matrix only in certain ω_1 and ω_3 regions and, therefore, to obtain the Fourier amplitude spectrum of, for example, of one cross-peak area.

   (c) Alternatively, it can integrate 3D FFT matrix only over ω_1 axis, so the result is similar to the pump-probe FFT, a 2D array of ω_3 vs. frequency wavenumbers.

5.4.3 Visualization software

The figures presented in the current work have been created following two different procedures. For the schematic figures (like fig. 2), a commercial app for Android devices was employed [51]; while experimental data and data obtained after analysis is visualized with its own developed Python software.

Python software for data visualization is constructed employing Numpy, Pandas and Matplotlib libraries. Additionally, for 2D maps representation, own developed colormaps are employed. Some warnings about data visualization have to be made at this point:

- Data from 2DES experiments, represented in two dimensional graphs of (ω_1, ω_3) for a fixed t_2, is showed with an interpolation to 200x200 points.

- Intensity of quantum beating maps, represented in two dimensional graphs of (ω_1, ω_3) for a fixed $\pm\omega_2$, might be presented with or without normalization. In the case of normalized maps, the method applied is explicit.

- Intensity of power FFT spectrum of the whole experiment or from some cross-peaks might be represented with or without normalization. Additionally, some parts of the spectrum might be omitted due to the interest of clarity. Modifications are also explicit in the cases where they are employed.

6 Results

6.1 Polarization-controlled 2DES

The real part of the total (rephasing and non-rephasing) 2D spectra is shown in figures 17 and 18. Figure 17 shows the time evolution of 2D spectra measured with AP polarization with Q_y and laser spectra poorly overlapped in fig. 17a and a bit better overlapped in fig. 17b. It has been chosen as representative three different t_2 times to study the dynamics: an early time, $60fs$; a medium time, $500fs$; and a late time, $2000fs$. Earlier times are omitted from the visualization and the analysis because of the pulse overlap artifacts [52].

Two-dimensional spectra of Chl a can be described in the following way. On the diagonal line, three peaks can be found; these correspond to the linear absorption spectra ones, Q_y, Q_x and Q_{y1} transitions (in the most common notation). As it was discussed in section 5.1, fast internal conversion from Q_x to Q_y in Chl a is supposed to happen within the first $50fs$ [33, 2] and, therefore, it is not possible to identify changes on the intensity of these diagonal peaks in present 2D spectra. However, a closer analysis can be done when analyzing the diagonal cross-section of the slides. This data is presented in Figure 19 for both AP experiments. Three diagonal cross-sections are shown for the first one, while only the $60fs$ one for the second.
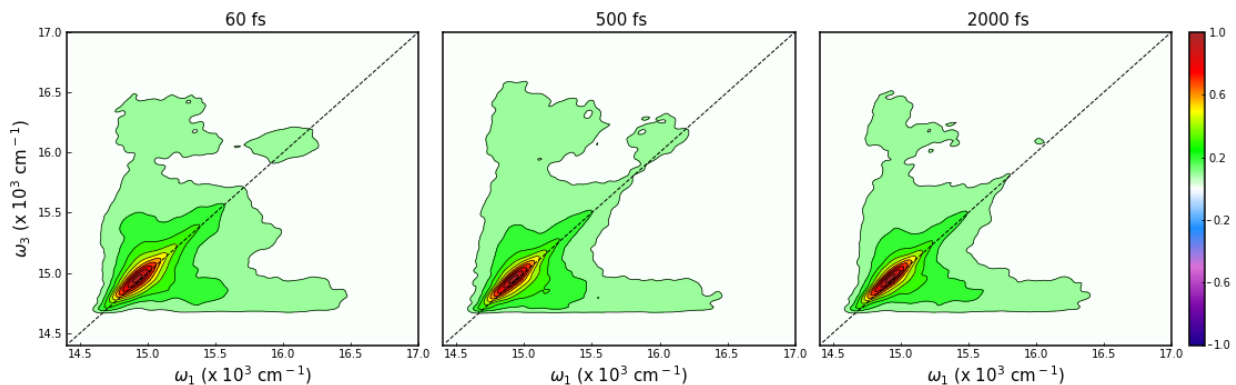
(a) First AP experiment, Q_y is not fully covered by laser spectrum.
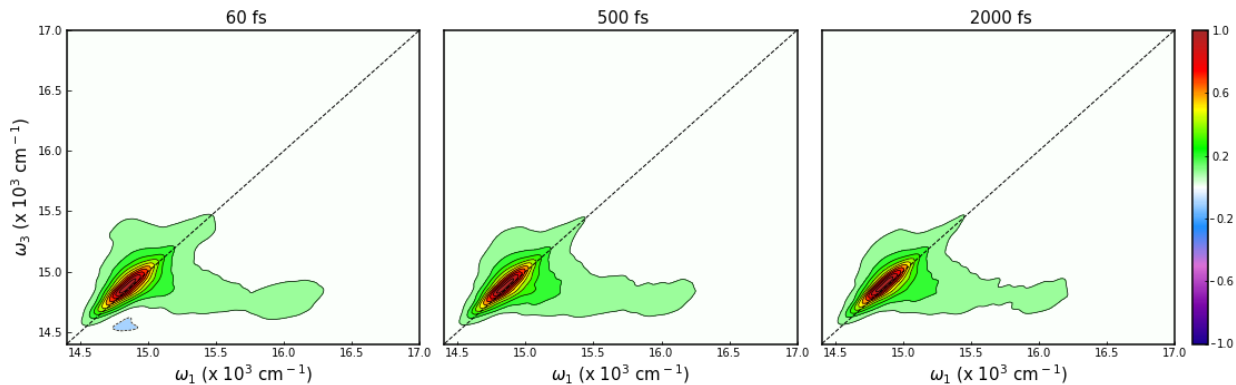
(b) Second AP experiment, Q_y is better covered by laser spectrum than previous experiment

Figure 17: 2DES spectra at different population times, t_2. The real component of the total (rephasing and non-rephasing) signal is shown. Dashed lines are drawn across diagonal of each 2D spectrum ($\omega_1 = \omega_3$). Every spectrum is normalized to their own maximum intensity point. Contour lines (solid for positive, dashed for negative signals) are spaced by every 5% of the maximum signal.
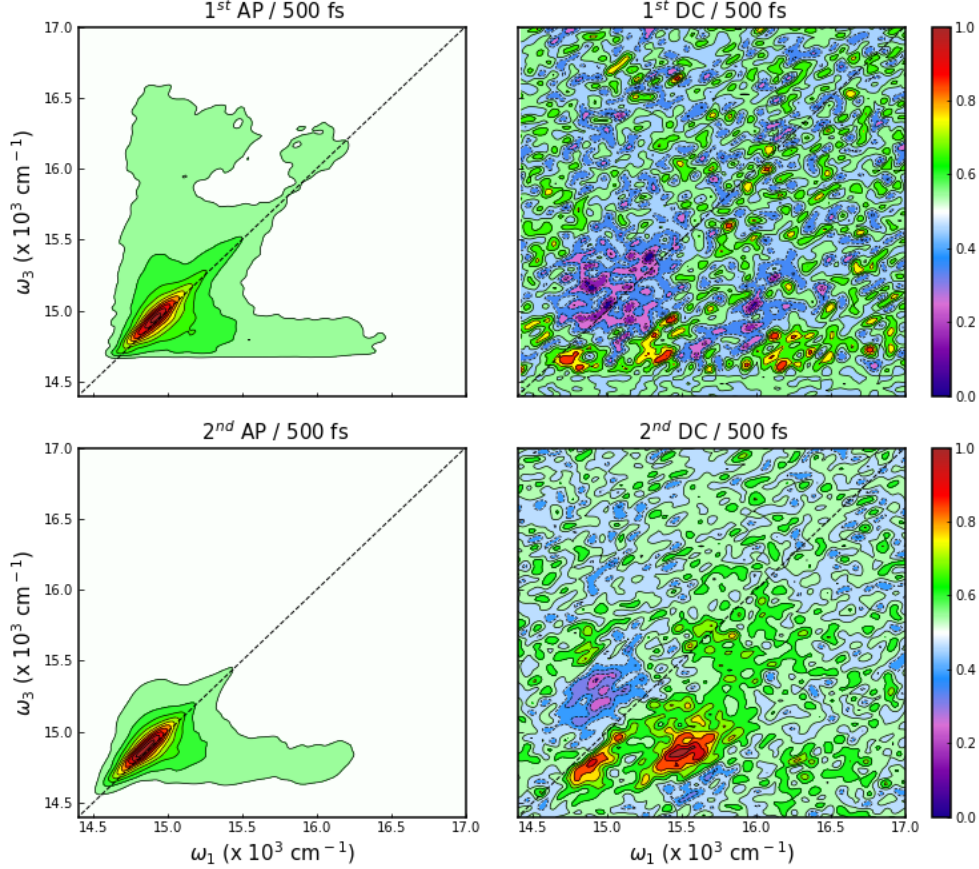
Figure 18: 2DES spectra at the population time $t_2 = 500 fs$. The real component of the total (rephasing and non-rephasing) 2D spectra measured under different conditions is shown. Top row corresponds to poor spectral overlap experiments, while bottom row corresponds to better spectral overlap experiments; left column correspond to AP experiments, while right column correspond to DC experiments. Dashed lines are drawn across diagonal of each 2D spectrum ($\omega_1 = \omega_3$). Every spectrum is normalized to their own maximum intensity point. In AP experiments, contour lines (solid for positive, dashed for negative signals) are spaced by every 5% of the maximum signal; while in DC experiments, contour lines are spaced by every 20% of the maximum signal due to the low signal-to-noise ratio.

For the first AP experiment, presented in Figure 19a, Q_x diagonal peak is not well visible. This corresponds to the expected fast internal conversion process. It is hidden in the "mountainside" of Q_y transition, which is slowly losing intensity. Q_{y1} transition is visible at $60 fs$, but it is not visible at later times, showing a slower evolution than Q_x transition. Q_y is present at similar intensities on its low energy part, but it slowly loses intensity in the high energy slope part.

One effect that the shift of laser spectrum has is the change of relative intensities of the three transitions. Q_y transition has now much more intensity than the other two and, therefore, the features of Q_x and Q_{y1} transitions are more hidden. This can be seen in Figure 19b, where these peaks are not visible at the earliest time of $60 fs$.

The effect of the shifted laser can also be noticed when comparing top row spectra and bottom row spectra in Figure 17. The higher intensity of Q_y diagonal signals hides, in some way, the rest of the features when normalizing the 2D spectra. As for the rest, in general, the probability of appearance of a certain signal is related to the number of photons of certain energy that interact with the matter in the proper way.
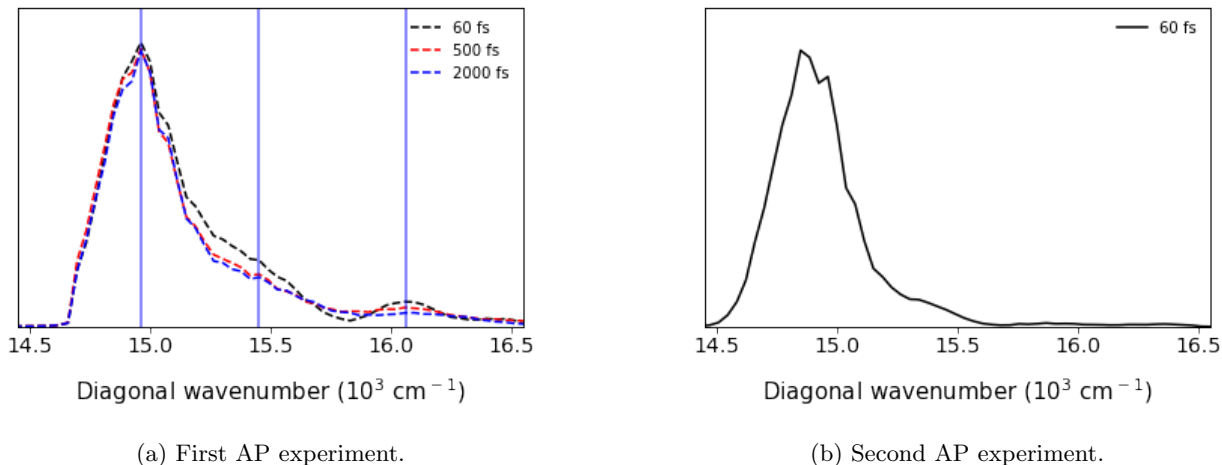
(a) First AP experiment. (b) Second AP experiment.

Figure 19: Diagonal cross-sections of AP experiments. In subfigure 19a, three slides at $t_2 = 60, 500, 2000 fs$ have been taken; while in subfigure 19b, only one spectrum at $t_2 = 60 fs$ has been taken.

Therefore, the laser shift allows new pathways to happen because it is covering now the low energy part of Q_y transition. In the same way, a laser shift might block pathways that involve high energy transitions, but this effect is not visible in our experiments.

Continuing with the analysis of the Chl a dynamics observed in 2DES spectra, it seems to be very salient in terms of visible signals. The growth of the cross-peaks in the 2D spectra is really fast, according to the fast internal conversion and, therefore, it is not tracked in the experiments. There is no raise of new peaks or disappearance of older peaks as t_2 goes on. Time traces of some diagonal and cross-peaks are found in Figure 21, where the fast character of the internal conversion makes it impossible to observe the expected early exponential dynamics. However, when it comes to coherent or incoherent dynamics, some parts of 2D spectra have associated multi-exponential dynamics and oscillatory behaviour. The results of the analysis of these features are presented in the next section.

Multiple cross-peaks above and below the diagonal are expected, as the considered system is only composed of a single molecule [53]. Due to the employed laser spectrum, which does not cover well Q_y transition, in the first AP experiment, cross-peaks are more visible; we can clearly see them between Q_y and Q_x and Q_y and Q_{y1}. Cross-peaks between Q_x and Q_{y1} are not visible under the diagonal, but seem to be visible above it in earlier times.

The presence of the signals from ESA pathways on cross-peaks areas might be possible; therefore, they could reduce or hide other cross-peaks, due to their negative amplitude. In order to consider them, excited states in the B band have to be taken into account. The lower-energy excited state of it has an energy of $23148 cm^{-1}$ at room temperature, and $22222 cm^{-1}$ at low temperature. The energy difference between Q transitions and that state is of the order of $6000 - 7000 cm^{-1}$; hence, it is not covered by the employed laser spectrum. When considering the higher-energy excited state of B band, the energy difference between it and Q_y state is of the order of $15000 cm^{-1}$; so it is somewhat covered by laser spectrum. When considering energy difference between Q_x and that state, the obtained value is lower, around $14500 cm^{-1}$. This one is badly (or not at all) covered by our laser spectrum.

Because of this, in the first AP experiment, it is not possible to go through ESA pathways, the laser spectra simply does not have the needed energy for that. Nevertheless, in the second AP experiment, the laser shift allows new pathways, and it is possible to observe how upper positive cross-peaks disappear under the new laser conditions. In Figure 18 they are not visible, but, when inspecting non-interpolated data, it is possible to observe the negative value of the upper cross-peak between Q_x and Q_y states, attributed to ESA

29

(a) 500fs slide of second AP experiment

(b) Time traces of the highlighted point in second AP experiment.

(c) 500fs slide of second DC experiment

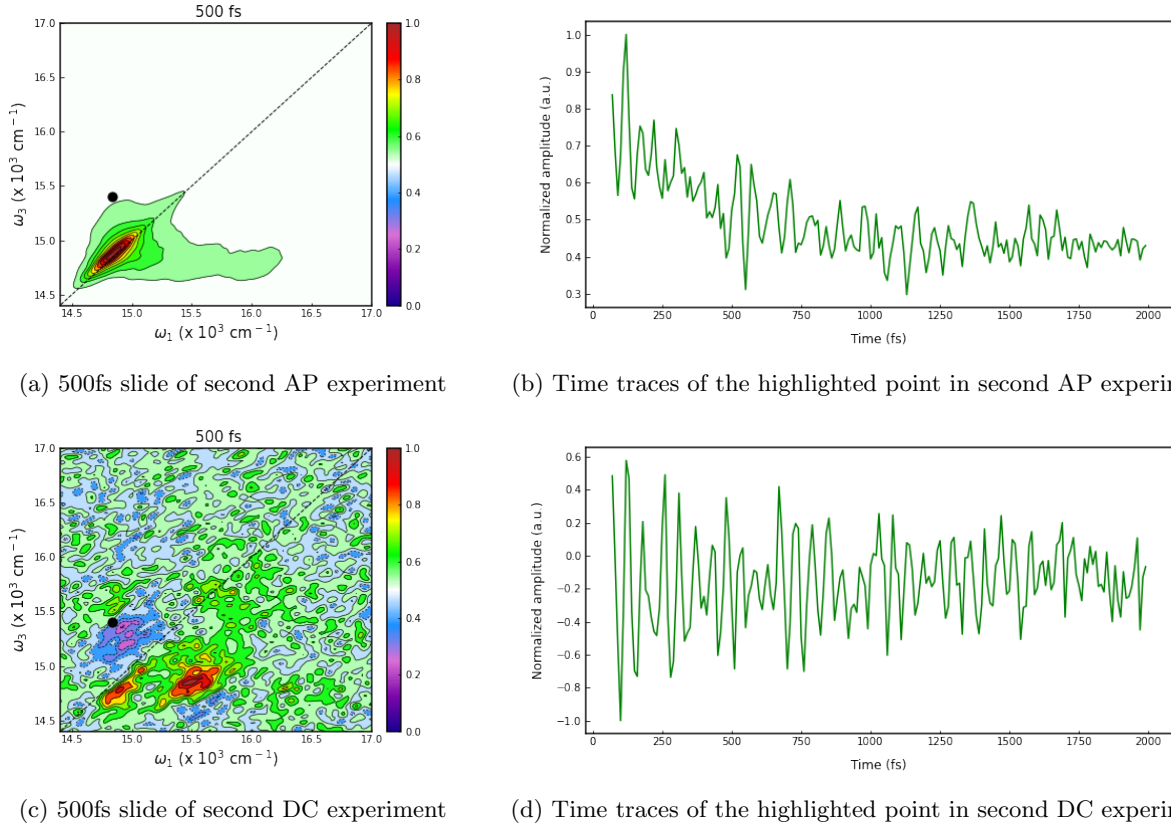(d) Time traces of the highlighted point in second DC experiment.

Figure 20: Extracted time traces from the experiments with Q_y better covered by laser spectra. Coordinates where present time traces have been extracted correspond to the upper cross-peak between Q_y and Q_x transitions, at $\omega_1 = 14840 cm^{-1}$ and $\omega_3 = 15400 cm^{-1}$. These coordinates are highlighted with a black point in their respective 2D spectra.

signals. However, their amplitude is still very weak.

Another important fact observed here is that the transition energies between states, when determined with 2DES, do not match perfectly with transition energies determined with a linear absorption spectrometer. These energies are, respectively for Q_y, Q_x and Q_{y1}, approximately $14950, 15400$ and $16100 cm^{-1}$ in 2DES; while they are $14773, 15347$ and $16031 cm^{-1}$ in linear absorption spectroscopy. This fact is attributed to the limited laser spectrum employed in the experiments. As it does not cover Q_y transition perfectly, it might cause a shift of energy transitions in 2D spectra.

In Figure 18, a comparison of both AP and DC 2D spectra can be made. A really large suppression of most signals is achieved with DC polarization-control. As it was previously described in section 4.6, while AP polarization realize all the signal pathways, DC polarization suppresses most of the signals, including the energy transfer and Frank-Condon vibrational coherence signals [3]. Because of this, only transitions with non-parallel dipole moments can lead to the rise of beating coherence signals. While the strongest DC signal is expected for an angle of 90° [11, 52], the angle between Q_y and Q_x transition dipole moment is somewhat around 70°. Therefore, electronic beatings and beatings excited via vibronically coupled Q_y and Q_x transitions will survive the DC polarization control. The analysis of vibronic coupling in Chl a is therefore not made from the 2DES spectra, but from the coherence beating signals.

(a) 500fs slide of second AP experiment.

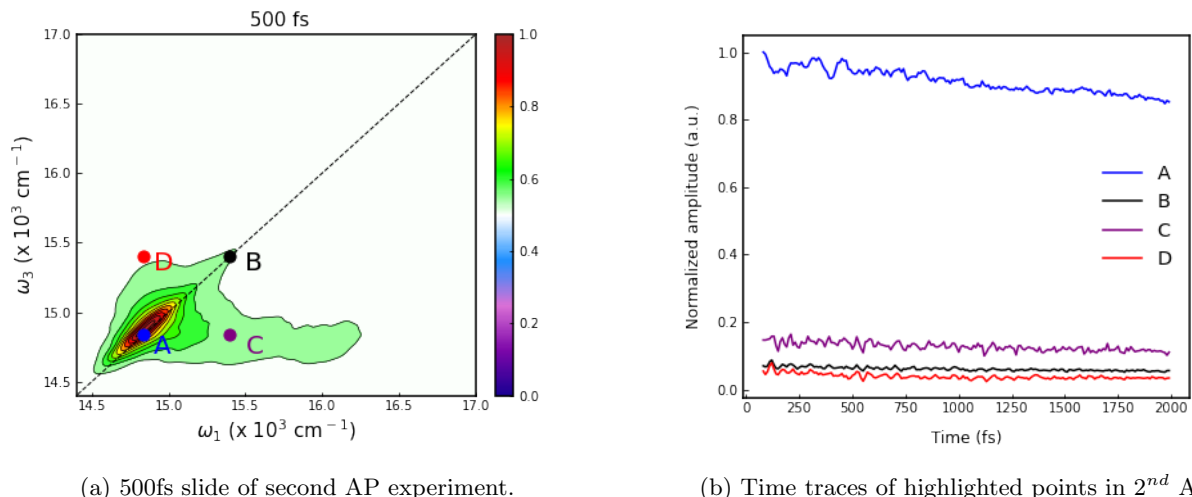(b) Time traces of highlighted points in 2nd AP.

Figure 21: Figure 21a shows the total AP spectrum at the 500fs population time. Figure 21b shows the 60fs-2000fs population time of the kinetic traces from the highlighted points: Q_y diagonal point (A), Q_x diagonal point (B), lower cross-peak between them (C) and upper cross-peak between them (D). Time traces are normalized to the maximum amplitude point of A values. It is not possible to observe either fast decay of higher energy diagonal peak (B) or fast rise of the cross-peak bellow diagonal (C) in accordance to the expected fast internal conversion. Slow decay of lower energy diagonal peak, A, is associated with the response of the solvent polar environment [54].

6.2   Coherence beatings and oscillation maps

Incoherent and coherent dynamics are present in 2DES spectra, and their graphical representation can be found on figures 20 and 21. A few important features can be noted in Figure 20. First of all, exponential decay signal is present in the AP time traces, but it is completely suppressed with DC polarization-control. Second, coherent or oscillatory dynamics are present in both experiments. Purely Franck-Condon vibrational coherences are completely suppressed in DC experiments and, therefore, the intensity of beating signals is lower. In Figure 20 amplitude intensities are normalized, which is why this feature can not be observed there.

In Figure 21, the experimental data points to the same conclusion regarding internal conversion: it has to happen earlier than what the used 2DES experimental set-up can track. Slow decay of signals is visible, specially in lower energy diagonal peak A, which is associated to the response of the solvent polar environment [54].

In our molecular system, rephasing and non-rephasing contributions provide basically the same information [13]. Therefore, only analysis of the rephasing part of the experiments is performed. Multi-exponential fitting is performed in every point, subtracting the kinetics from the population time evolution traces for the four experiments. Complex FT is performed on the residuals, obtaining the spectral positions and amplitudes of different coherence oscillation modes, with both positive and negative values ($\pm\omega_2$). Detailed procedure is explained in section 5.4.2.

Figure 22 shows the Fourier transform amplitudes extracted from all the experimental data points, so the result is the Fourier amplitude spectrum of each whole experiment. However, signal-to-noise ratio is low in all the experiments, specially in the AP ones where no signals are blocked due to the employed polarization. Estimation of real value of signal-to-noise ratio after a FFT might be tricky if the frequency values, which should and should not have amplitude, are not known. In order to avoid this problem when exploring FT frequencies, complex FT amplitudes are extracted from only the cross-peak regions of Q_x and Q_y transitions. The result of this procedure for second AP and DC experiments (after laser shift) is shown in Figure 23.

31

Frequencies of the most prominent peaks found in this analysis are explored and analyzed in the beating maps. Integrated FT is performed in Q_y-Q_x cross-peaks areas, whose limits are: $14580 - 15000cm^{-1}$ for ω_1, $15200 - 15900cm^{-1}$ for ω_3 in the upper cross-peak; and $15200 - 15900cm^{-1}$ for ω_1, $14580 - 15000cm^{-1}$ for ω_3 in the lower cross-peak.

Additional integrated FT can be done in the Q_y-Q_{y1} cross-peak area. The frequency limits are $14580 - 15000cm^{-1}$ for ω_1, $15900 - 16350cm^{-1}$ for ω_3 in the upper cross-peak; and $15900 - 16350cm^{-1}$ for ω_1, $14580 - 15000cm^{-1}$ for ω_3 in the lower cross-peak. Results of the integrated FTs for the 2nd AP and DC experiments are presented in Figure 24.

Finally, the resolution of the results is as follows:

- The 2D maps have a resolution of $\Delta\omega_1 = \pm 50 \ cm^{-1}$ and $\Delta\omega_3 = \pm 60 \ cm^{-1}$.

- The Fourier amplitud spectra have a resolution of $\Delta\omega_2 = \pm 20 \ cm^{-1}$.
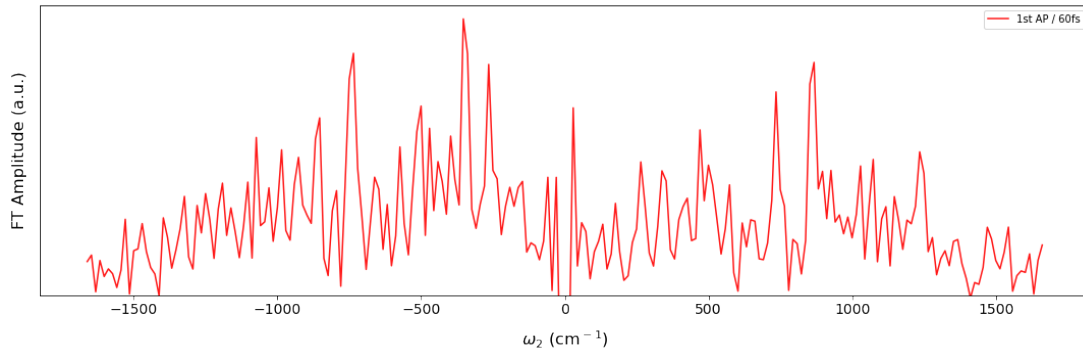
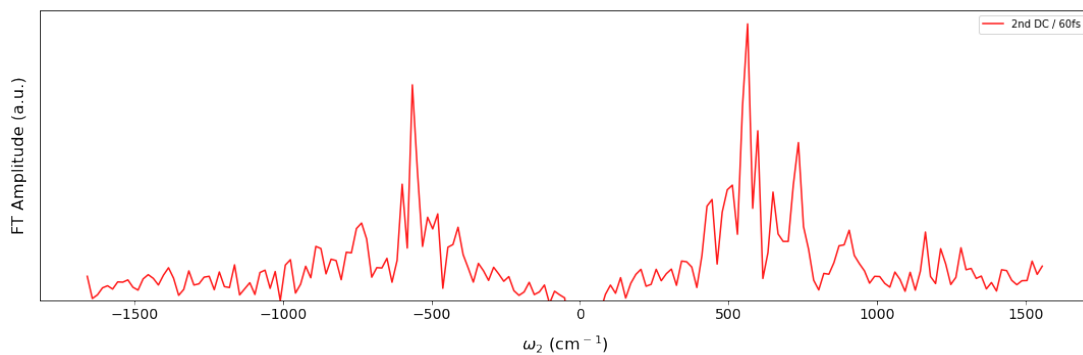(a) 1st AP Fourier amplitude spectrum
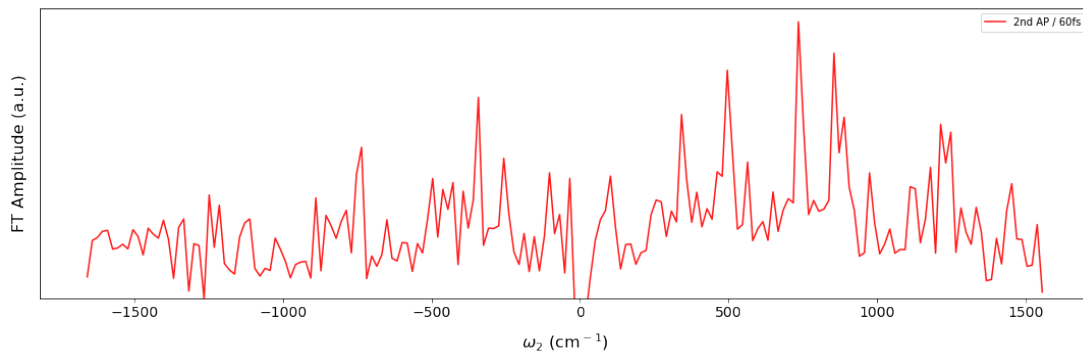
(b) 2nd AP Fourier amplitude spectrum
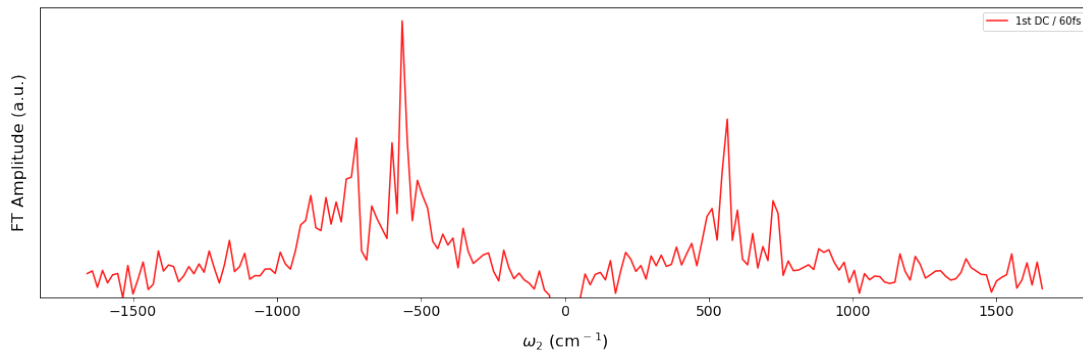
(c) 1st DC Fourier amplitude spectrum

(d) 2nd DC Fourier amplitude spectrum

Figure 22: Fourier amplitude spectrum of each experiment after integrating the complex FT data over the whole experimental data points of each one. Normalization is made in every graph to their respective maximum amplitude value.
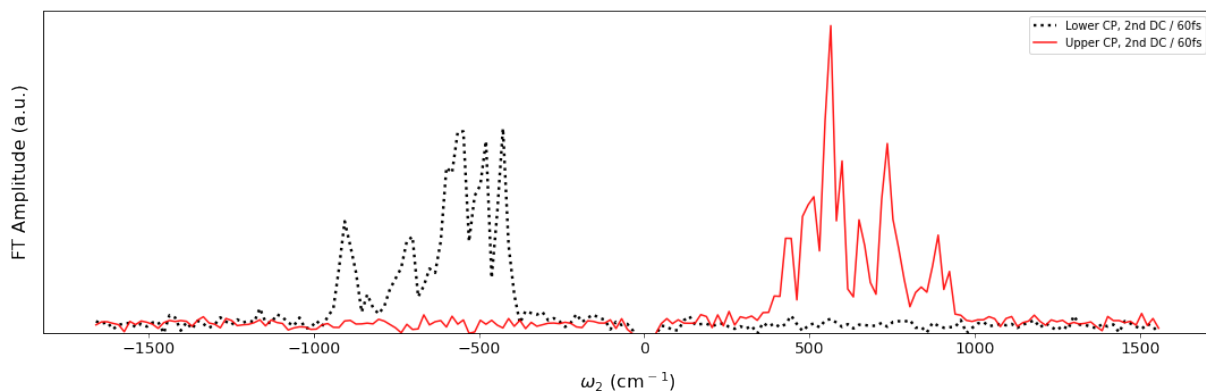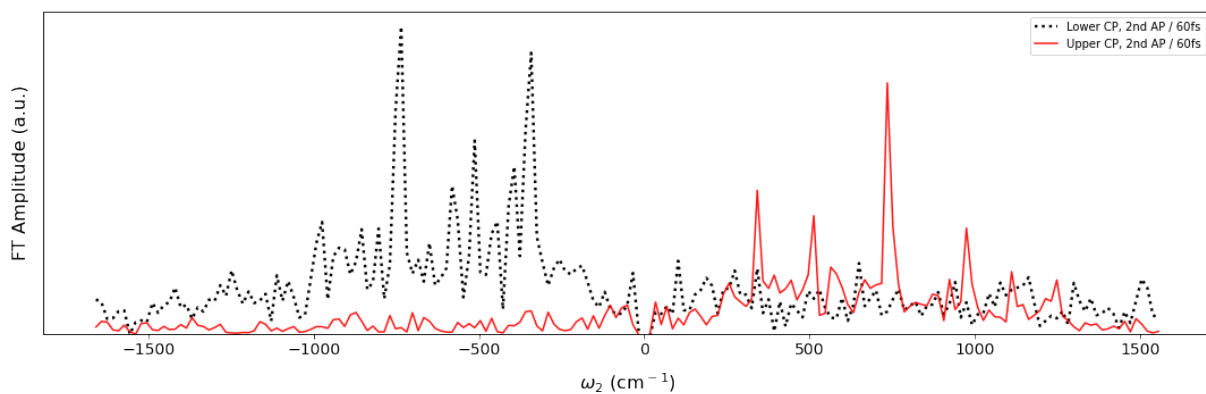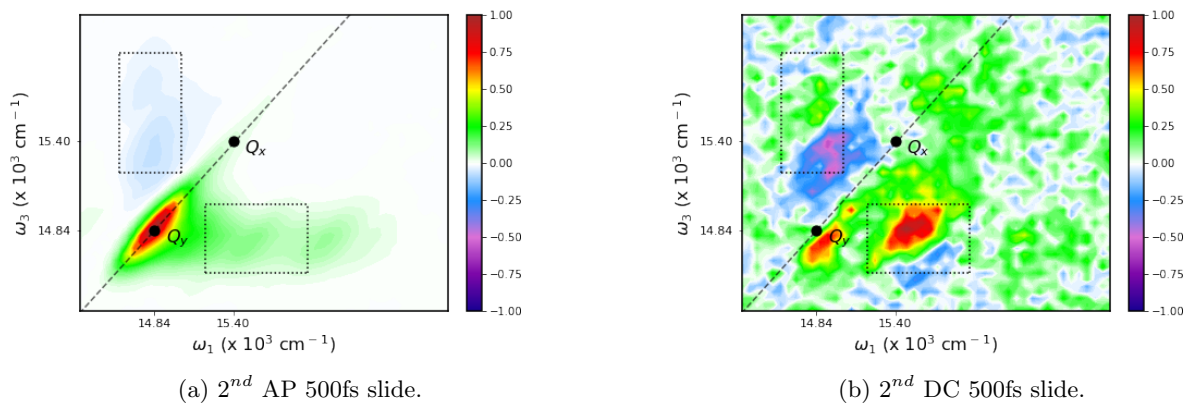
(a) 2nd AP 500fs slide.

(b) 2nd DC 500fs slide.

(c) Lower vs. upper cross-peak FT amplitudes in 2nd AP experiment.

(d) Lower vs. upper cross-peak FT amplitudes in 2nd DC experiment.

Figure 23: Fourier amplitude spectrum of each experiment after integrating the complex FT data over either lower or upper Q_y-Q_x cross-peak data points, as highlighted in subfigures 23a and 23b. Normalization is made in every graph to the maximum amplitude value of their respective experiment (either AP or DC, taking both upper and lower cross-peak regions into account).
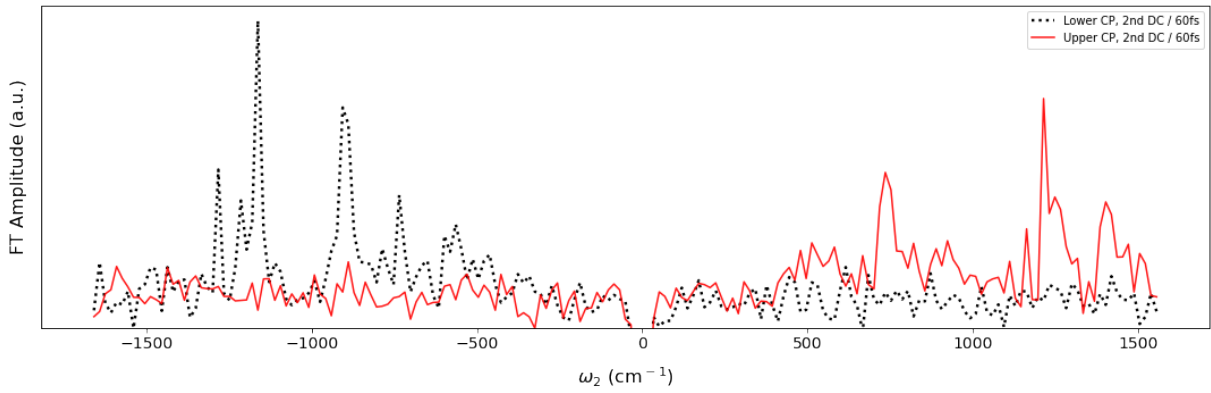
(a) 2nd AP 500fs slide.

(b) 2nd DC 500fs slide.

(c) Lower vs. upper cross-peak FT amplitudes in 2nd AP experiment.

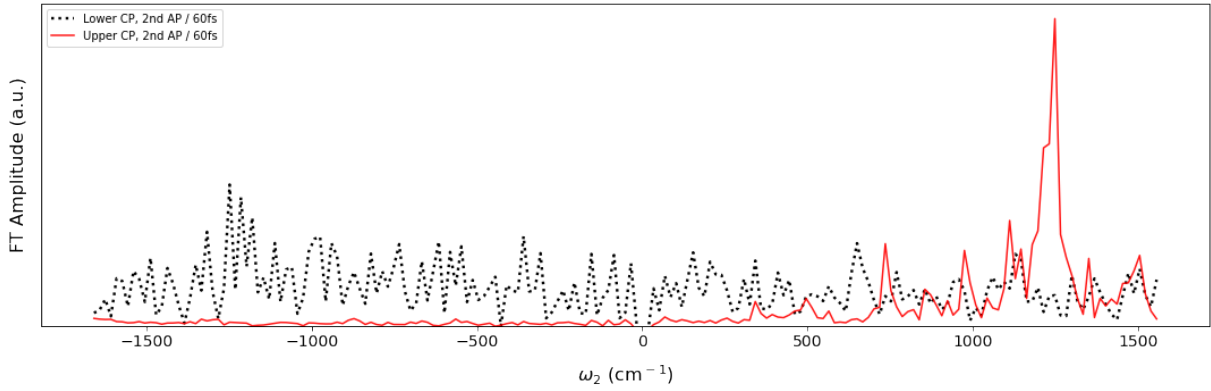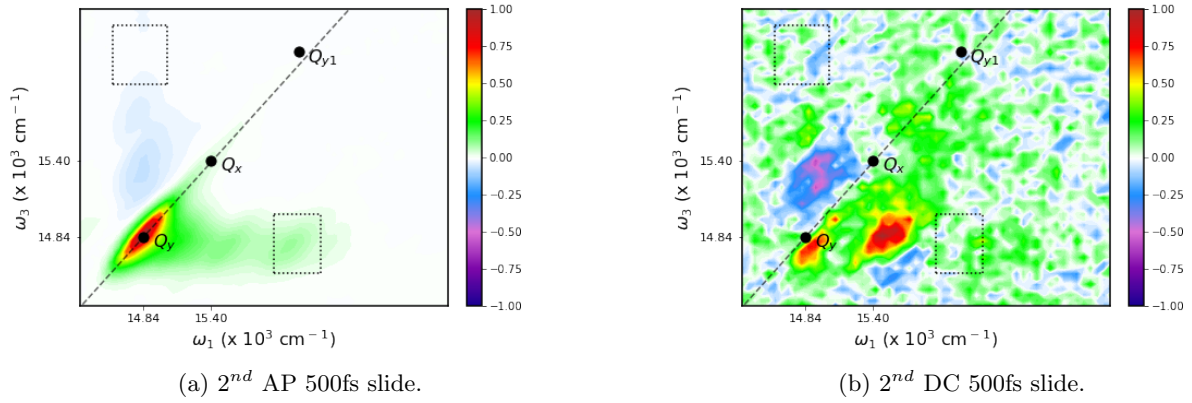(d) Lower vs. upper cross-peak FT amplitudes in 2nd DC experiment.

Figure 24: Power spectra of each experiment after integrating the complex FT data over either lower or upper Q_y-Q_{y1} cross-peak data points, as highlighted in subfigures 24a and 24b. Normalization is made in every graph to the maximum amplitude value of their respective experiment (either AP or DC, taking both upper and lower cross-peak regions into account).
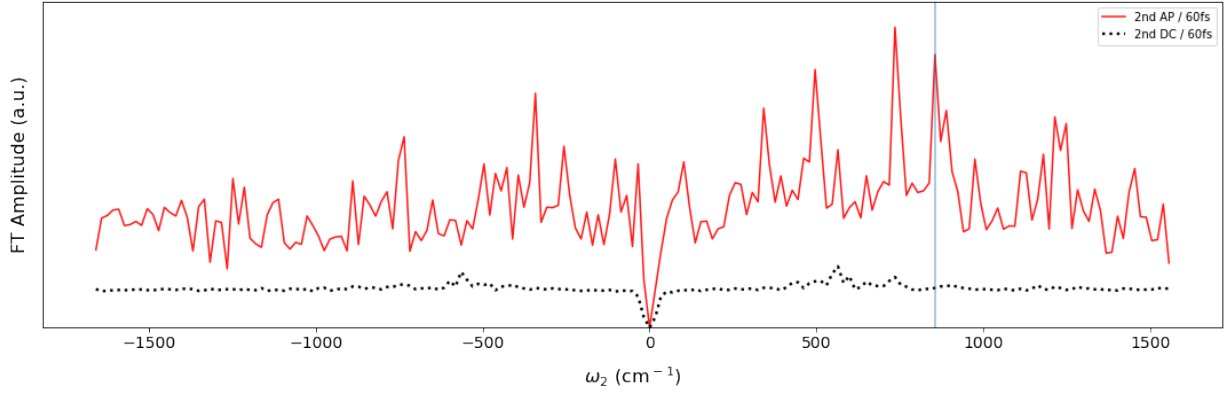
(a) 2nd AP and DC experiments for the full integrated FT.
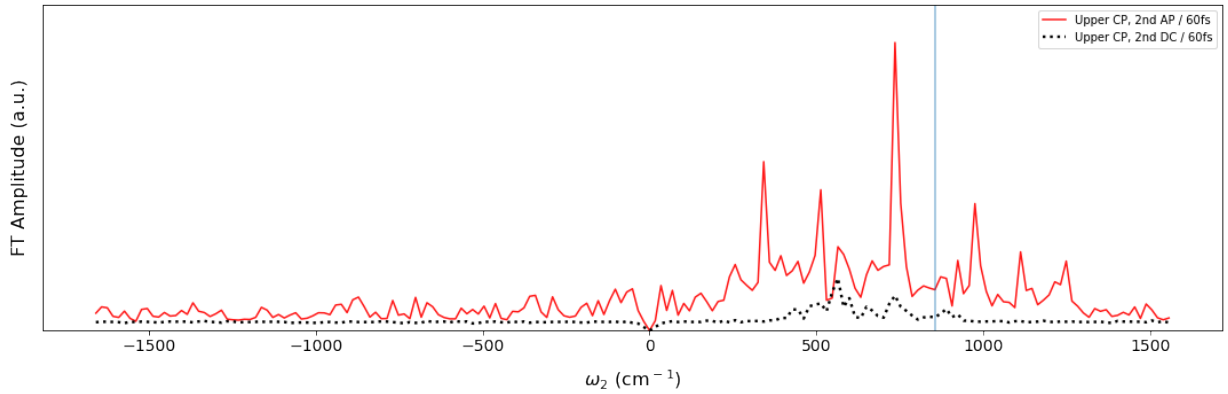
(b) 2nd AP and DC experiments for the upper cross-peak integrated FT.

Figure 25: Comparison of absolute amplitudes between 2nd AP and DC experiments for the total experimental area 25a and upper cross-peak area 25b integrated FT. Vertical blue line highlights the impulsively excited 1-propanol Raman mode at $855cm^{-1}$ [55], which might be used to estimate the suppression factor when employing DC polarization control).

Due to potential experimental imperfections, such as misalignment of polarizators or possible light depolarization when it goes through the optical elements, it is appropriate to make an estimation of suppression factor of unwanted signals when applying DC polarization control.

To do that, it is possible to evaluate the coherence signal amplitude ratio between the AP and DC experiments of impulsively excited 1-propanol Raman mode at $855cm^{-1}$ [55] when integrating FFT values over the full ω_1 and ω_3 values. This value is highlighted in Figure 25. This kind of estimation was employed previously by Bukartė et al. [3] when working with Chl c_1.

However, another different approach to evaluate the suppression ratio is employed here. The procedure is to analyze the ratio between absolute intensity values of AP and DC 2DES spectra. When focusing on the maximum intensity value of $500fs$ slide for every experiment, which corresponds to the center of Q_y diagonal peak, the suppression ratio found is 75.2 for the first experiments and 130.3 for the second ones.

Analysis of beating frequencies is focused in the $\pm(400 - 800)cm^{-1}$ region for different reasons. First, the energy difference between Q_y and Q_x states is $560cm^{-1}$ and the integrated FT covers the area between their cross-peaks. Second, the strongest amplitudes for beating frequencies in DC experiments are found in this region, where coherences excited via vibronically coupled transitions are expected. Nevertheless, some interesting beating frequencies are found outside these margins. Beyond the lower limit, beating frequen-

cies are found in AP experiments that are not present in the DC ones; and above the upper limit, beating frequencies are found when integrating over the full experimental data, pointing to coherences where the named Q_{y1} transition is involved. In the next few pages, figures with a full series of pictures of beating maps of every experiment are present. Visualization method for beating maps is explained in every case, as it is different for each figure. We mostly focus on the experiments after laser shift is done, as it has a better resolution. Beating maps of the first experiments are only used to compare some features.

Beating maps of most prominent beating amplitudes for 2nd DC experiment (upper and lower cross-peaks integrated areas).
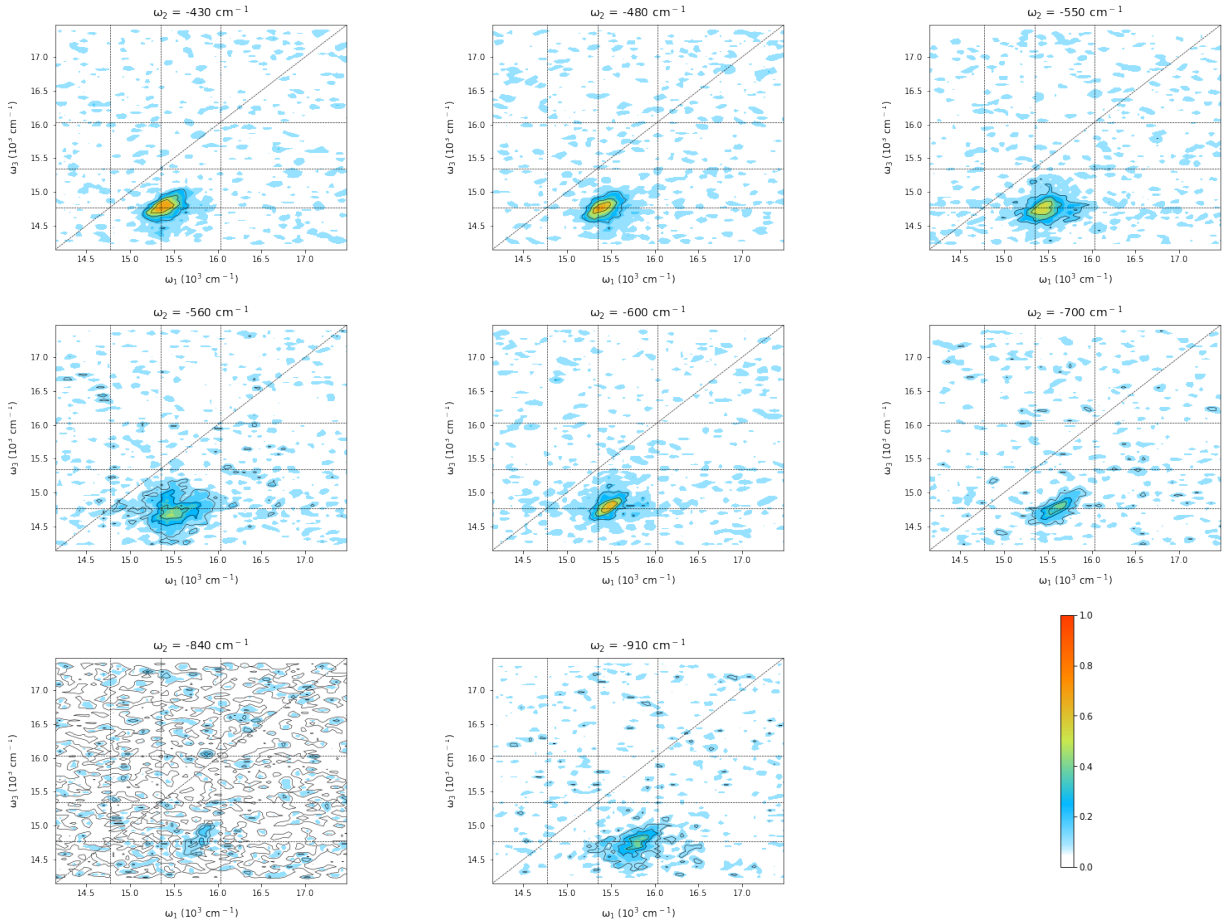

Figure 26: Beating maps of most prominent negative beating amplitudes for 2nd DC experiment (lower cross-peaks integrated areas). Normalization method for amplitudes is done to the maximum value of the most prominent beating frequency at $560 cm^{-1}$. Colormap code is found in the last subfigure.
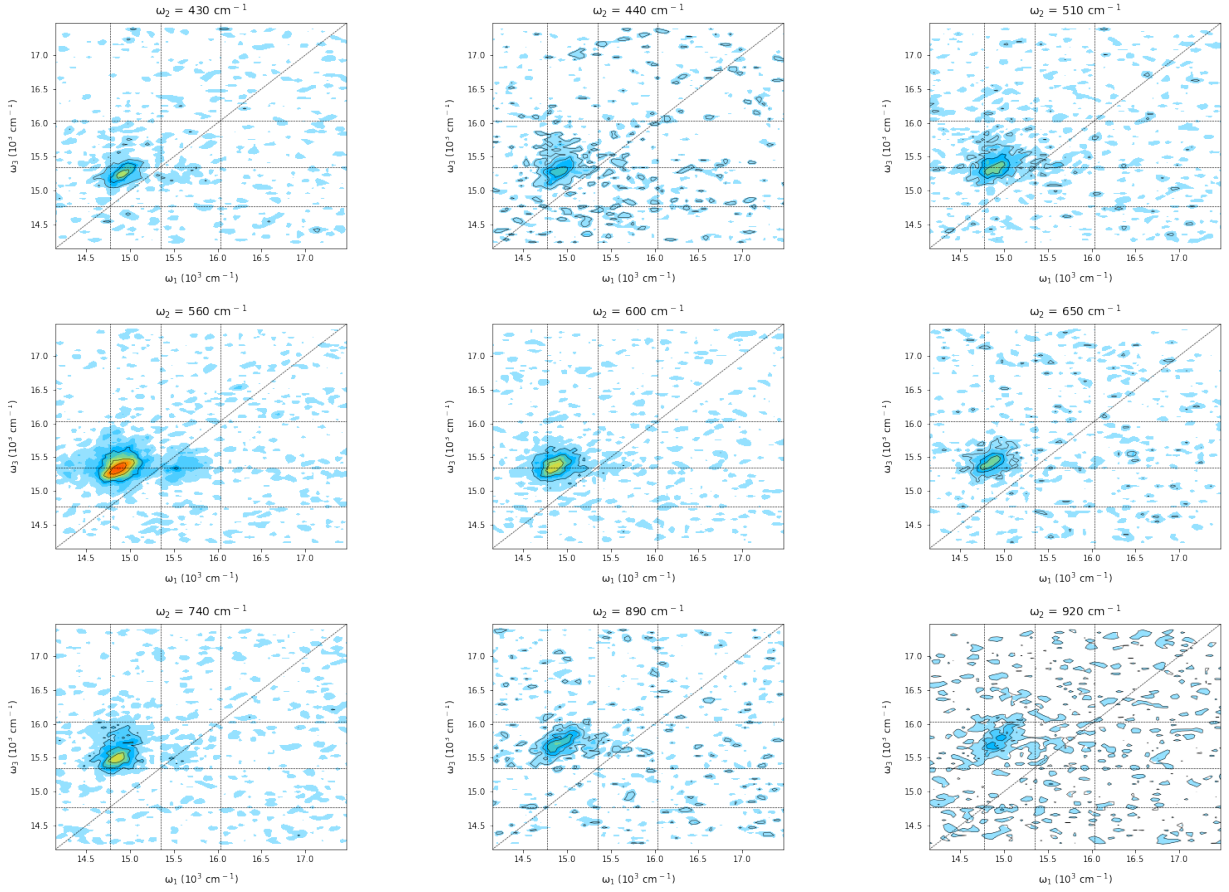
Figure 27: Beating maps of most prominent positive beating amplitudes for 2nd DC experiment (upper cross-peaks integrated areas). Normalization method for amplitudes is done to the maximum value of the most prominent beating frequency at $560 cm^{-1}$. Colormap code is found in the last subfigure of Figure 26.
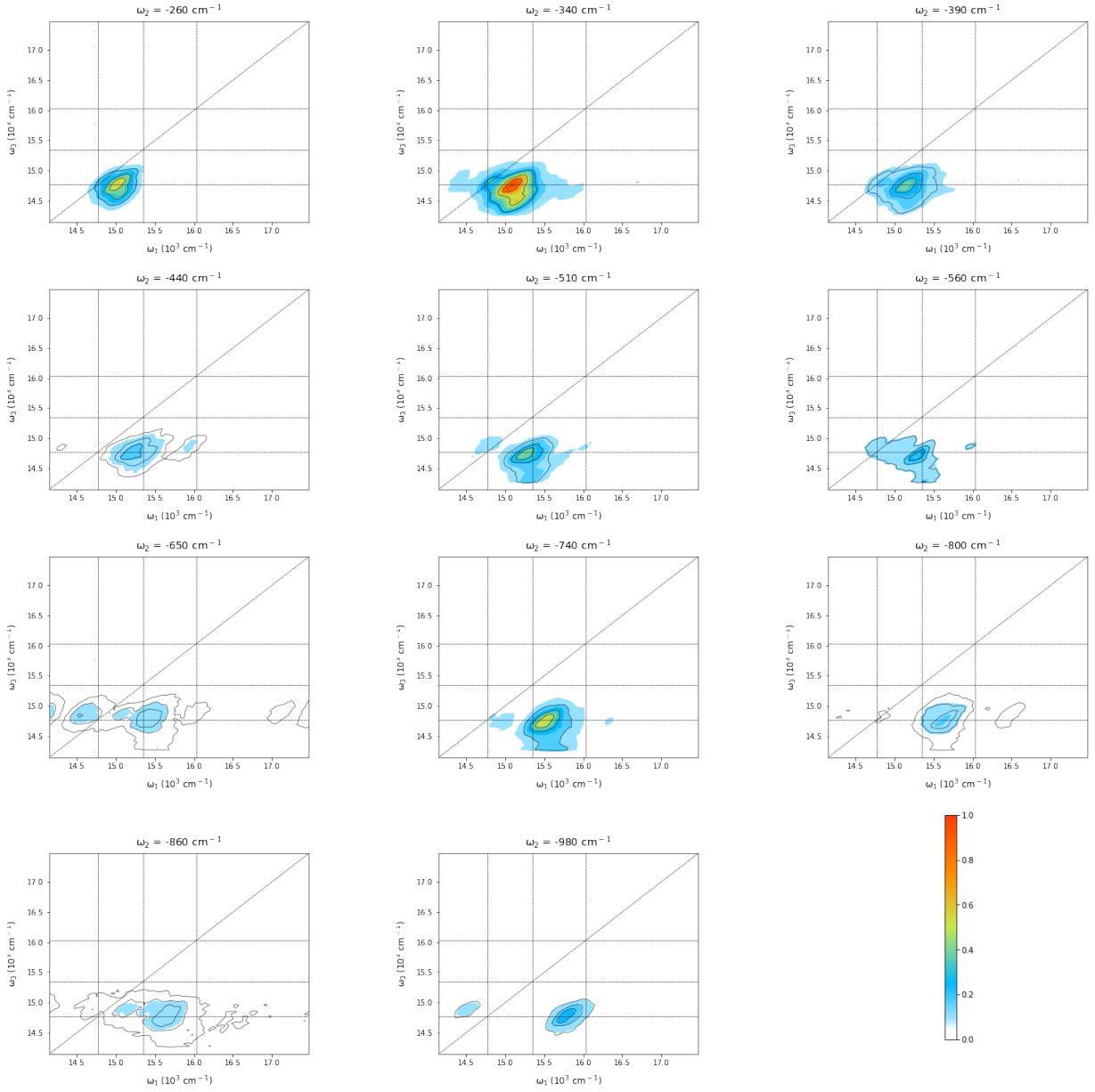
Figure 28: Beating maps of most prominent negative beating amplitudes for 2nd AP experiment (lower cross-peaks integrated areas). Normalization method for amplitudes is done to the maximum value of the most prominent beating frequency at $-340cm^{-1}$. Colormap code is found in the last subfigure.
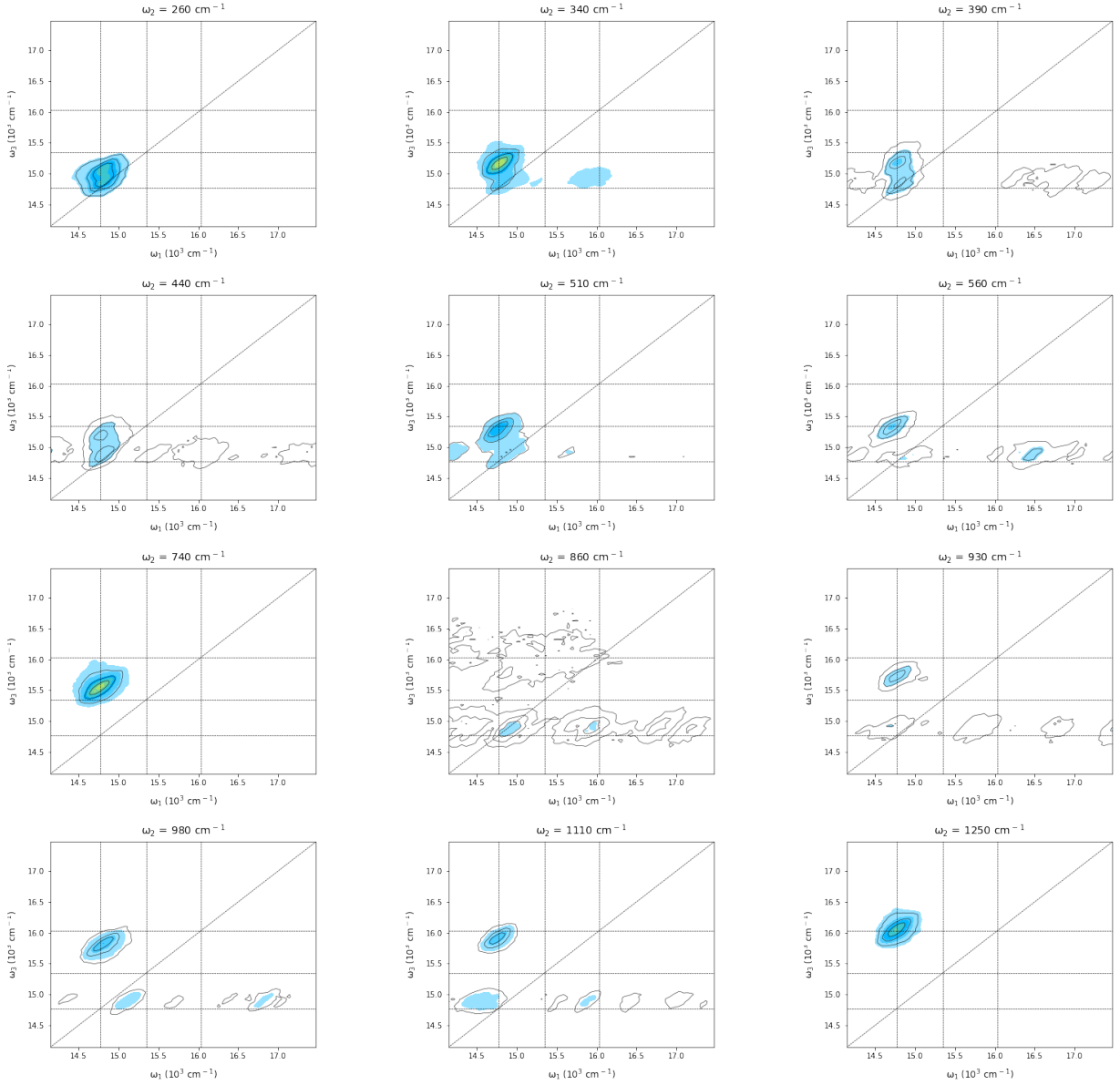
Figure 29: Beating maps of most prominent positive beating amplitudes for 2nd AP experiment (upper cross-peaks integrated areas). Normalization method for amplitudes is done to the maximum value of the most prominent beating frequency at $-340cm^{-1}$. Colormap code is found in the last subfigure of Figure 28.

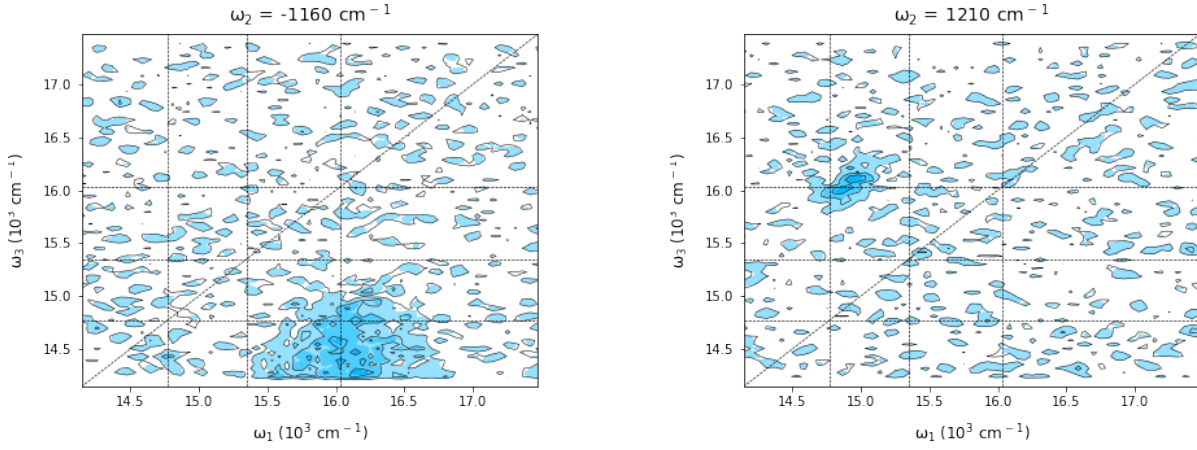*Beating maps for most prominent high frequency peaks.*

- 2nd DC experiment

Figure 30: Beating maps of most prominent high-energy beating amplitudes for 2nd DC experiment (Q_y-Q_{y1} cross-peaks integrated areas). Normalization method for amplitudes is done to the maximum value of the most prominent beating frequency at $560cm^{-1}$. Colormap code is found in the last subfigure of Figure 26. Although more beating frequencies are find, noise beating maps are omitted here.
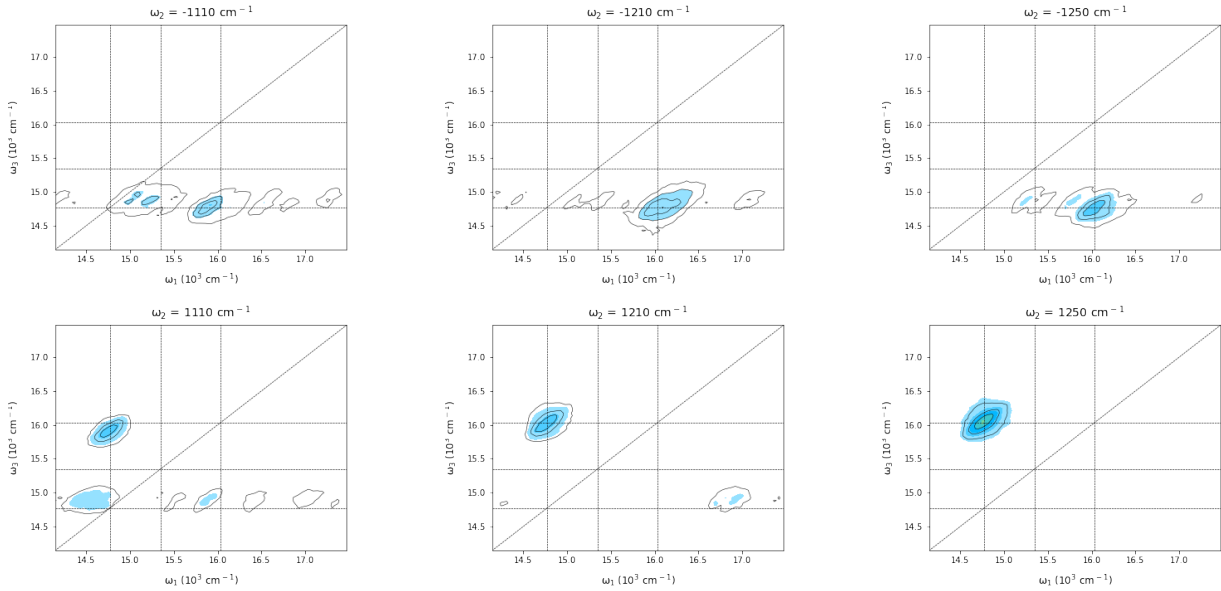
- 2nd AP experiment

Figure 31: Beating maps of most prominent high-energy beating amplitudes for 2nd AP experiment (Q_y-Q_{y1} cross-peaks integrated areas). Normalization method for amplitudes is done to the maximum value of the most prominent beating frequency at $-340cm^{-1}$. Colormap code is found in the last subfigure of Figure 28.

6.3 Discussion

Internal conversion in Chl a

Multiple studies of Chl a explore the energy relaxation between Q_x and Q_y states with different techniques [2, 33, 36, 37], generally finding that the internal conversion within $Q_x \rightarrow Q_y$ is extremely fast, and that it occurs within 50fs [2, 33]. Under the used experimental conditions it is not possible to track this energy relaxation in Chl a, as the first 50fs of experimental measurements are not reliable. Neither is present an observable decay in the Q_x diagonal peak nor a rise of lower Q_y-Q_x cross-peak in the time traces after 50fs. Nevertheless, internal conversion has to be present and, according to the data from the pointed previous selected studies, conclusion taken here is that it has to happen within the first 50fs. As internal relaxation is associated to faster times than the ones chosen for the coherences analysis (from 60fs onwards), presence of electronic coherences on complex Fourier analysis is discarded.

Reimers et al. related the internal relaxation with coupling strength and resonance between the unperturbed energy gap between the Q states and the vibrational frequency [1]. Therefore, the fast internal relaxation, besides being due to the small energy gap between Q states in chl a, $875cm^{-1}$, it might be attributed to a strong vibronic coupling between those states.

Some notes about probed pathways

Beating maps can appear due to the presence of different types of coherences: vibrational, electronic or vibronic coherences. Moreover, different types of coherences, such as vibrational coherences, can be excited via pathways that involve vibronically coupled states. The main goal of the work is to demonstrate vibronic coupling in Chl a, and this can be achieved with the identification of coherences excited via vibronically coupled states. Analysis of beating maps whose frequencies have the most prominent amplitudes after integrated FT is the way to identify origin of the observed coherences. This analysis of beating maps is mainly based on the theory described by Butkus et al. [13], incorporating complex analysis of the frequencies detailed elsewhere [11, 56] and described in Figure 9.

Pathways which contribute to oscillating signals that will appear in beating maps are described in Figure 10 for vibrational coherences, and in Figure 11 for either electronic/vibronic coherences. One important fact has to be noted here regarding the full analysis of the beating maps: laser spectra is truncated in the lower energy part of Q_y transition. While this fact favours the rise of coherences between Q_y and Q_x states, it blocks a lot of pathways involved in vibrational coherences. In fact, it blocks all the pathways that require low-energy transitions, which are marked with a "-1" circled in red in fig. 10. When applying this signal "filter" to the theoretical beating maps one conclusion is achieved: vibrational and electronic/vibronic beating maps look exactly identical.

This led to the laser spectrum shift that was done after the first set of experiments. It could allow the light-matter interaction to go through some vibrational pathways in order to distinguish coherence types. The effect of laser spectrum shift will be analyzed in the lower diagonal peak of two different AP signals: $\omega_2 = \pm 340 cm^{-1}$ and $\omega_2 = \pm 560 cm^{-1}$.

Lower diagonal peak is present in both positive and negative beating maps. In that position, SE pathway leads to an oscillating contribution during t_2 with a **positive** phase and, therefore, if it is allowed, it will be present in the positive frequency beating map. In the same spot, GSB pathway leads to an oscillating contribution during t_2 with a **negative** phase and, therefore, if it is allowed, it will be present in the negative frequency beating map. For these pathways, needed laser intensities are collected in Table 3 and beating maps are present in Figure 32 with their respective Feynman diagrams.

If needed intensities are analyzed, transitions marked in red might not be allowed. Laser spectrum simply might not have the necessary intensity to excite such transitions. Laser profile employed in the experiments can be found on Figure 33. It is clear that laser beam employed in the first experiments does not have
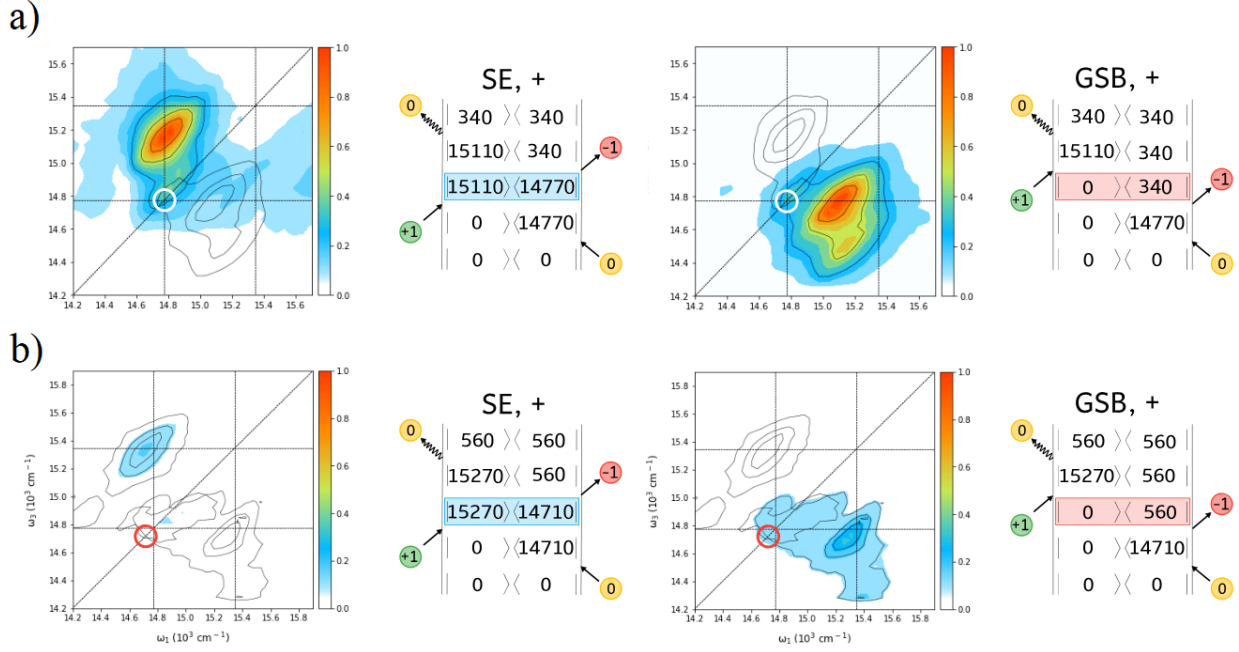
Figure 32: Beating maps for a) $\pm 340 cm^{-1}$ and b) $\pm 560 cm^{-1}$. Left maps are the positive ones, while the ones at the right are the negative. Circled areas on the maps point where one specific signal, the lower diagonal one, is expected for vibrational coherences. SE is expected for the positive beating map, while GSB is expected for the negative one. Color code is similar than the one employed on figures 10 and 11.

Number of interaction	1 (ω_1 cm^{-1})	2 (cm^{-1})	3 (cm^{-1})	4 (ω_3 cm^{-1})
Frequency of beating map (cm^{-1})				
+340	14770	15110	14430	14770
−340	14770	14430	15110	14770
+560	14710	15270	14150	14710
−560	14710	14150	15270	14710

Table 3: Laser intensities needed for having signal in the lower diagonal peak of the beating maps at $\omega_2 = +340 cm^{-1}$ (SE), $\omega_2 = -340 cm^{-1}$ (GSB), $\omega_2 = +560 cm^{-1}$ (SE) and $\omega_2 = -560 cm^{-1}$ (GSB). Color code is similar than the one employed for Feynman diagrams. Transitions in red color might not be covered by laser spectrum.

photons with frequency of $14500 cm^{-1}$ or lower than that. Therefore, all pathways which involve low energy transitions are not happening there. Things are more tricky with the second experiments, because laser beam have some photons of frequency $14500 cm^{-1}$, but not very much when compared with the other parts of the laser spectrum profile. Therefore, some transitions that require energy around $14400 - 14500 cm^{-1}$ can happen, but not with much intensity. Graphical representation of this situation can be found on Figure 34, where new signals are present in the $-340 cm^{-1}$ beating map after laser spectrum shift.

However, as we increase the absolute frequency of the beating map, the necessary energy for the low energy transition is even lower. For $\omega_2 = \pm 560 cm^{-1}$ maps, frequencies of $14150 cm^{-1}$ are needed. For $\omega_2 = \pm 740 cm^{-1}$ maps, frequencies of $14000 cm^{-1}$ are needed. Then, after the laser spectra shift, the beam might have energy to excite some transitions and, therefore, unveil some vibrational coherences; but it definitely does not have enough energy to unveil *all* of them.

Since Q_y transition is located, in 2D experiments, at $14840 cm^{-1}$, it is possible to estimate which tran-
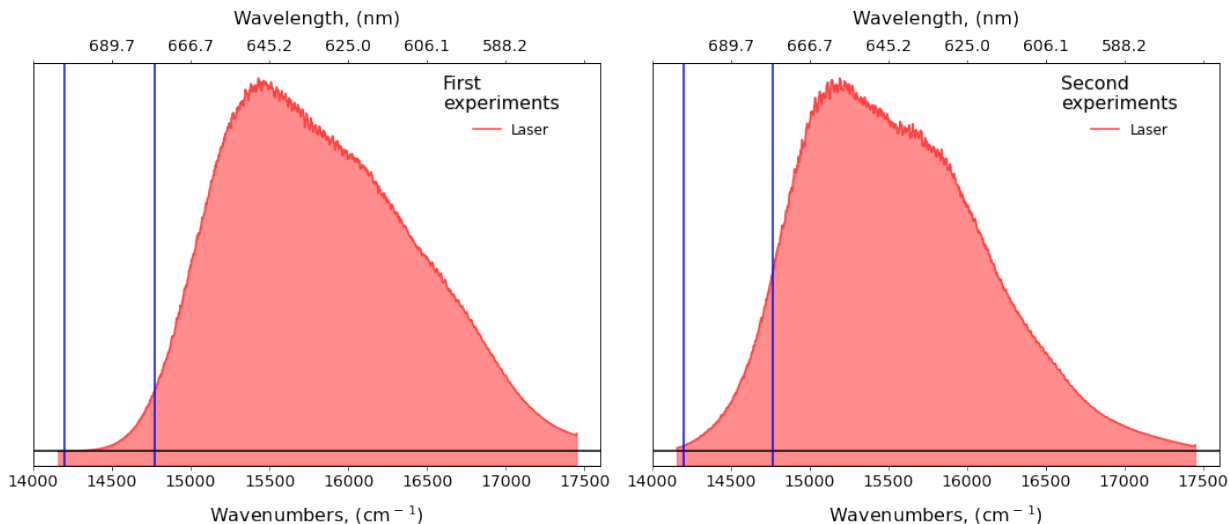
Figure 33: Laser spectra profile employed in the first experiments (left) and in the second experiments (right). Blue lines mark the center of the Q_y transition (right one) and the lower energy limit that can record CCD camera due to its calibration (left one).

sitions can have or can not have chair pattern with the lower energy limit of laser spectrum. In the first experiments, an estimation of $14840 - 14600 = 240cm^{-1}$ or lower is found. At such frequencies, proximity to the principal diagonal makes impossible to observe the chair pattern; therefore, no chair patterns should be expected. In the second experiments, an estimation of $14840 - 14250 = 590cm^{-1}$ or lower is found. However, the number is not solid, and the absence of chair patterns around $500 - 600cm^{-1}$ beating maps is not enough to conclude the vibronic origin of coherences.

Nevertheless, this situation is not a problem at all when exploring the existence of vibronic mixing. When employing DC polarized-control 2DES, coherence signals that arise from the superposition of states with parallel transition dipole moments, like Frank-Condon vibrational coherences, are completely suppressed [3] and, as previously discussed, electronic coherences are not considered. Therefore, despite not having enough confidence on what we are observing, if vibronic coherences or vibrational coherences excited via vibronically coupled states, the presence of signals in $\pm600cm^{-1}$ area in DC experiments is, by itself, a proof of vibronic mixing. This provides a direct observation of vibronic coupling between the Q_y and Q_x states, as predicted by Reimers et al. [1].

The most important fact here, and the reason why it is possible to observe vibronic coupling between these states under DC polarization-control, is that state mixing results in a shift of transition dipole moment orientation of involved states. The mixed character of Q_x transition with a vibrational mode of Q_y makes it possible to excite, employing light pulses that have a 90° degrees angle between their polarization, some pathways that, otherwise, would be suppressed. Such pathways include ground state vibrational coherences and excited state vibrational coherences with non-parallel dipole moments, observed in the DC experiments.

Positive beating maps

According to Butkus et al. [13], oscillating signals with positive wavenumbers above diagonal in the rephasing experiments point to the existence of excited state coherences. This signals can clearly be observed after integrated FFT in Figure 22 for the total area and in Figure 23 for upper and lower cross peaks. In the case of the second experiments, their beating maps are found in figures 27 and 29 for DC and AP polarization-control, respectively. It can be observed that in the specific region of interest, $+(400-800)cm^{-1}$, prominent peaks are found.
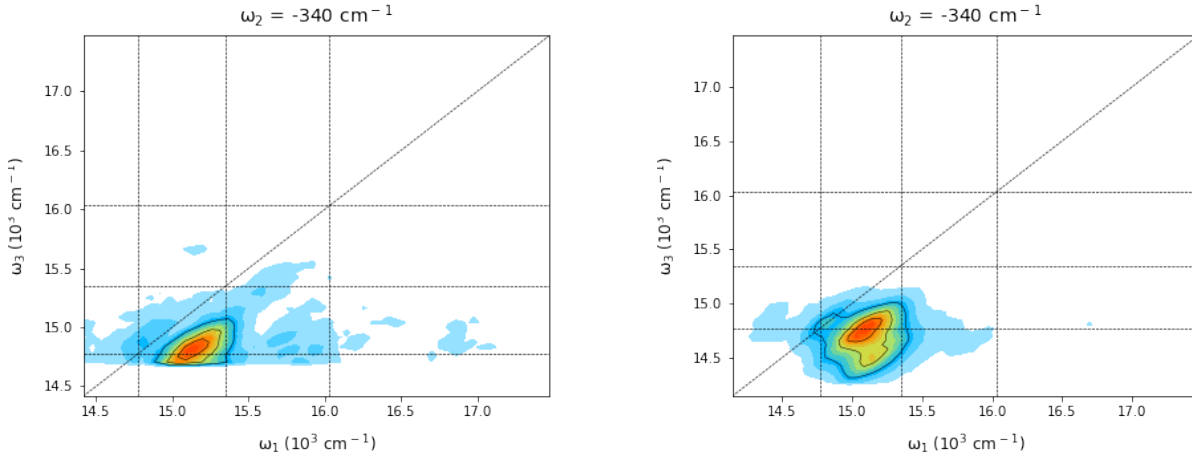
Figure 34: Difference on the pattern observed on the same frequency beating map ($-340cm^{-1}$) for the two AP experiments. At the left, AP beating map before laser shift; at the right, AP beating map after laser shift. It is a good example of how the cut of laser spectrum in the lower energy part might affect the proper assignment of the signal, hiding some features if laser photons do not have the necessary frequency. In this case, the laser shift unveiled the vibrational pattern, but for higher energy beating maps, the laser shift is not able to do it.

In the specific region of interest, AP experiments find peaks at $+440, +510, +560$ and $+740cm^{-1}$ beating frequencies, while DC experiments find peaks at $+430, +440, +510, +560, +600, +650$ and $+740cm^{-1}$. $+440cm^{-1}$ and $+510cm^{-1}$ seem to be vibrational coherences excited via vibronically coupled states, while the other frequencies might have the same origin or be purely vibronic coherences. As the laser spectrum does not cover lower-energies, no conclusions regarding their origin can be extracted here. Some beating peaks, such as $+600cm^{-1}$ or $+650cm^{-1}$ are not visible in AP experiments. This might be due to the small absolute amplitude value that they have. They are hidden in AP experiments, but when DC polarization-control acts, they become visible.

Various peaks are obtained in the interest area but, due to the laser cut, it is hard to come up with a conclusion about their origin. However, the presence of a large number of positive peaks is consider as an evidence of having more than one vibrational Q_y state leading to vibronic mixing with Q_x state.

Other peaks of interest are found in the lower frequency area. Under $400cm^{-1}$, AP experiments find peaks at $+100, +150, +260, +340$ and $+390cm^{-1}$. When studying their beating maps, signal contribution in the diagonal is observed, something that points to their assignation as Frank-Condon vibrational coherences in the Q_y excited state. This statement is reinforced with the fact that these signals are not present in the DC experiments, as they are completely suppressed. Expected vibronic mixing is happening between Q_x and some vibrational modes of Q_y, so coherences that do not involve such vibrational levels of Q_y will not be present in DC experiments.

Discussion of high energy frequency beatings is given later in the current section.

Negative beating maps

According to Butkus et al. [13], oscillating signals with negative wavenumbers bellow diagonal in the rephasing experiments point to the existence of ground state coherences, but excited state coherences can be present as well. Excited state coherences lead to beating signals with identical amplitude at positive/negative wavenumber, as the pathways involve transitions with exactly the same energy, but with opposite phase

temporal evolution during population time t_2 (see Feynman diagrams in figures 10 and 11). Ground state bleaching coherences, on the other hand, lead to beating signals with only negative values, as it is impossible to describe pathways that involve GSB and that generate positive superposition of states in rephasing 2D experiments. Therefore, when comparing negative vs. positive peak amplitudes, only two situations are expected: either their values are symmetric or negative peaks are more prominent due to GSB contributions.

This situation is clearly seen in AP integrated FT peaks. Negative beating maps with $-340, -510, -740$ and $-980cm^{-1}$ have more intensity than their respective positive counterparts. The rest of the most prominent negative peaks, whose values are shown in Figure 28, do not have a prominent positive counterpart. This situation is in accordance with the presence of GSB contributions, which break the symmetric amplitude foreseen by SE contributions.

Such situation is more complex in DC experimental data. $-430, -480, -700$ and $-910cm^{-1}$ are more prominent than their positive counterparts; while $+440, +510, +560, +650, +740, +890$ and $+920cm^{1}$ are more prominent than their negative counterparts. In some signals, the counterpart is directly not present, and there is an absence of signals in $+480, +700$ and $910cm^{-1}$ for positive frequencies; and in $-440, -510, -650, -740$ and $-890cm^{-1}$ for negative frequencies.

Although DC polarization control is used, it is still possible to obtain the coherences in the ground state that are excited by the impulsive Raman process. This situation is allowed due to the presence of vibronically coupled transitions. The phase value of these oscillations is always negative; therefore, they can explain most prominent negative peaks, or the presence of negative peaks without their respective positive counterpart. However, the opposite situation is more complex to explain, as there are not "additional" pathways for positive beating frequencies.

Regarding this, Bukartė et al. [3] had similar cases with Chl c_1, and they attributed the observed coherences to the superposition of vibrational states that are not involved in vibronic mixing but have appreciable Huang-Rhys factors. They can be excited via vibronically mixed transitions and be observed even in DC experiments.

Due to the same problem with limited laser spectra, no new information can be attributed to negative beating maps that was not previously attributed when analyzing the positive ones for the complementary signals. Only one exception seems to be found on $-560cm^{-1}$ beating map. Its positive counterpart beating map does not show any signals on the diagonal, but it does have some intensity of signal on the diagonal and on the below lower cross-peak, situation that points to a vibrational coherence excited via vibronically coupled transitions.

Analysis of higher frequency beatings

Higher frequency prominent peaks are found in the experiments. Whilst they are not present when the integration area is a cross-peak area between Q_y and Q_x states; they are specially visible when the chosen area to integrate is a cross-peak area between Q_y and Q_{y1} states. These peaks are presented in Figure 24.

Some selected beating maps for prominent frequencies are shown in figures 30 and 31. The intensity values of the signal in these maps are very close to noise values; therefore, little information can be extracted from them. Other evaluated frequencies do not show any signal. This is related to the fact that Fourier amplitude spectra, for higher frequency peaks, are obtained integrating only along upper or lower Q_x and Q_{y1} cross-peak areas; while beating maps have an associated noise that comes from the whole experimental data. Therefore, their features are mostly hidden at the noise level, as their intensities are much lower than the ones of Q_y-Q_x beating maps.

Oscillation frequencies of such beatings are similar to the energy difference between Q_y-Q_{y1} states, which is $1280cm^{-1}$ when determined with 2DES. As some of the beatings survive (or only are appreciable) in DC experiments, it is reasonable to follow the same argument line than with Q_y-Q_x cross-peak beatings, and
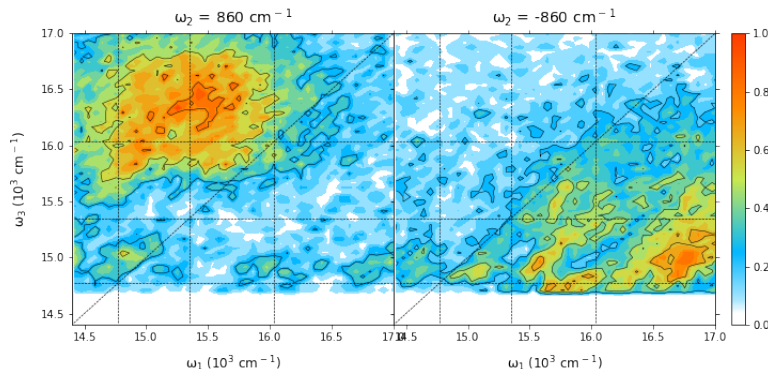
Figure 35: Beating map whose frequency matches the impulsively excited 1-propanol Raman mode at $855cm^{-1}$[55], which could be used to estimate the suppression factor when employing DC polarization control. Maps are taken from the first AP experiment and normalized to themselves.

conclude that they have to be the result of coherences excited via vibronically coupled transitions.

While Q_y and Q_x are better known and described in the literature, more controversy surrounds Q_{y1} transition. Here, it is going to be considered as the high-energy state that arises from the vibronic mixing between Q_x purely electronic state and some specific high energy vibrational states of Q_y [1, 3, 33]. In this way, Q_{y1} has the mixed character that makes transitions that go through it survive the DC polarization-control, and this character of Q_{y1} is experimentally observed here.

Regarding the frequency values of Fourier amplitude spectra, in the second AP experiment, clear positive frequencies are found at $+980, +1110, 1150, 1250$ and $+1350cm^{-1}$; but a very bad resolution makes impossible to identify negative frequency beatings. In the second DC experiment, clear negative frequencies arise at $-910, -1160, -1210$ and $-1280cm^{-1}$; and positive frequencies arise at $+1160, +1210, 1250$ and $1400cm^{-1}$. The presence of almost all of these peaks in the DC experiments point to the participation of Q_{y1} state in the formation of coherences.

Finally, special mention has to be made to the presence of the $860cm^{-1}$ signal in AP experiments. That frequency corresponds to the maximum intensity frequency point of the Raman spectra of 1-propanol [55], and it can be impulsively excited in 2DES experiments with AP polarization. Therefore, the presence of this signal in the integrated FT graphs or in the beating maps do not provide information about vibronic coupling in Chl a. Beating maps of that frequency can be found, for the first AP experiment, in figure 35

Vibronic mixing in Chl a

The analysis of DC polarization-controlled 2DES experimental data unveils a considerable number of beating frequencies. Although the origin of coherences that give rise to such frequencies is not clarified, one thing is clear: they have to be excited via vibronically coupled transitions. A large amount of these frequencies are found in the cross-peak area between Q_y and Q_x states, which points to conclude that Q_x transition is mixed, not with only one, but with a certain number of transitions to higher-energy vibrational states of Q_y.

Figure 36 presents a visual schematic approach to how coherences that involve vibronic mixed states in Chl a are generated on the DC experiments. Q_y and Q_x states are inseparable mixed, but the mixing character is stronger in the states that have similar energies. Therefore, while the character of purely electronic Q_y state or higher-energy vibrational states of Q_x remain similar; the mixing strongly affects the character of some high-energy Q_y states and purely electronic Q_x states, affecting some of their properties, such as their energy.

In Figure 36, the first light-matter interaction excites the system to the Q_y state, and the second light-

47

matter interaction to a vibronically-mixed state. After the two interactions, the system would be in the following superposition of states, $|(Q_x - Q_y)\rangle\langle Q_y|$, where $(Q_x - Q_y)$ denotes a mixed state as previously defined. That superposition of states evolves in time, and it can be detected as an oscillating signal.
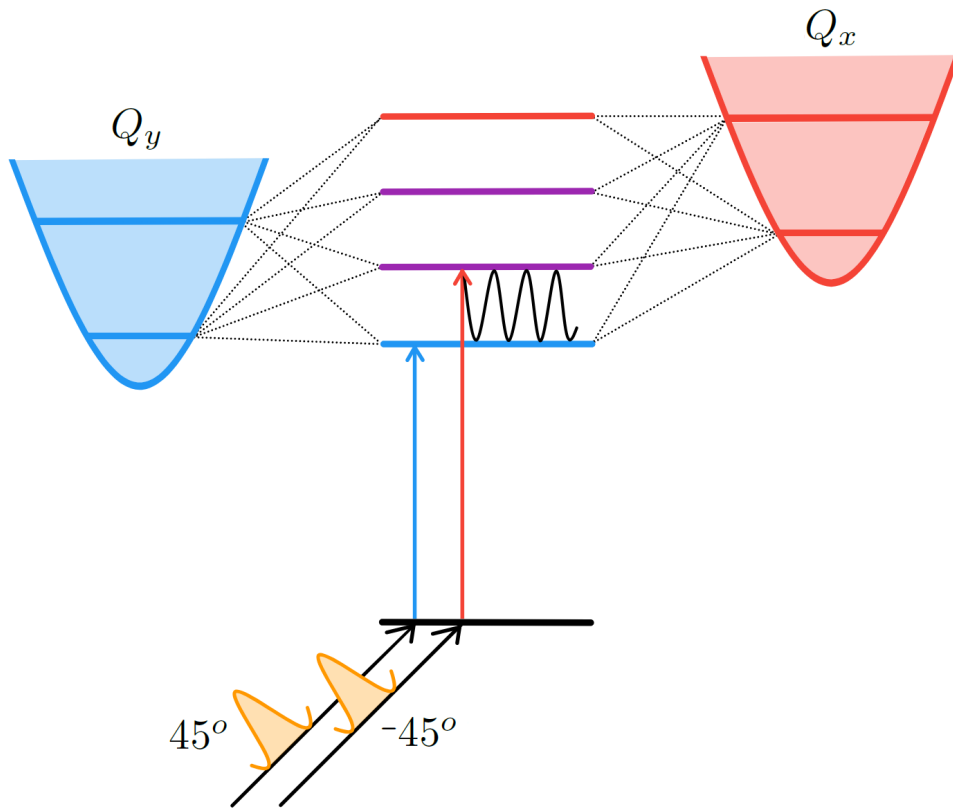

Figure 36: Visual schematic approach to how coherences that involve vibronic mixed states in Chl a are generated on the DC experiments. The first light-matter interaction excite the system to the Q_y state, and the second light-matter interaction to a vibronically-mixed state, generating the superposition of states. It evolves in time, and it can be detected as an oscillating signal.

7 Conclusions

The presence of vibronic mixing in chlorophyll-type molecules was purposed by Reimers et al. [1], who developed a complete vibronic coupling model for the chlorophyllides family of molecules. With the help of 2DES, some evidences of vibronic mixing have been found since then. This is what Song et al. [2] reported when studying the experimental transition dipole moment in Chl a. The direct observation of vibronic mixing was firstly done by Zigmantas and co-workers [3] in Chl c_1; they found a forest of active beating modes in DC polarized-control 2DES. They concluded that vibronic coupling in chlorophyll-type molecules should be a common feature, and that it should be taken into account when modeling their electronic and photo-physical properties regarding the photosynthetic function.

Here, methodology of Zigmantas and co-workers [3] is applied to Chl a, a more common system than Chl c_1. The aim was to observe the described property in an easy-to-obtain molecule, and the most common of the chlorophyllides family.

In agreement with previous studies, results of the performed experiments point to the same conclusion. Multiple and different coherences generated with 2DES experiments survive the DC polarized-control; therefore, their origin has to be either electronic or excited via vibronically coupled transitions. As demonstrated, under experimental conditions, only coherences excited via vibronically coupled transitions can give a rise to such coherences, and they are directly observable in the experiments. Therefore, we conclude that Q_x transition and some transitions to high-energy vibrational states of Q_y are vibronically mixed in Chl a. Moreover, due to the similarity of chlorophyllides, which exhibit comparable electronic structures featuring two main Q_y and Q_x bands, this vibronic coupling is strongly expected to be present in all the members of chlorophyll-like molecules.

The study of coherences that arise from the cross-peak regions between Q_y and Q_{y1} transitions discovers similar findings, as some oscillation modes also survive the DC polarized-control experiments. This fact points to characterize Q_{y1} as a high-energy vibronically mixed transition.

The study performed here attempts to unveil coherences excited via vibronically coupled transitions. However, due to some experimental characteristics, such as laser spectra profile, a deeper analysis of beating origins and vibrational modes that are responsible for the vibronic coupling are not done here. Future studies, with different experimental set-ups and better modelling of the system, might be able to provide deeper understanding of these questions.

In conclusion, the role of vibronic coupling in photosynthesis is not clarified yet, and an extensive debate over it is currently going on [54, 57]. However, qualitative and quantitative improved comprehension of vibronic coupling arises as a necessity, as it is demonstrated to be present in chlorophyll-like molecules, and it might play a key role in the photosynthetic functions.

References

[1] Jeffrey R. Reimers, Zheng-Li Cai, Rika Kobayashi, Margus Rätsep, Arvi Freiberg, and Elmars Krausz. Assignment of the q-bands of the chlorophylls: Coherence loss via qx - qy mixing. *Scientific Reports*, 3(1), 2013.

[2] Yin Song, Alexander Schubert, Elizabeth Maret, Ryan K. Burdick, Barry D. Dunietz, Eitan Geva, and Jennifer P. Ogilvie. Vibronic structure of photosynthetic pigments probed by polarized two-dimensional electronic spectroscopy and ab initio calculations. *Chemical Science*, 10(35):8143–8153, 2019.

[3] Eglė Bukartė, Anja Haufe, David Paleček, Claudia Büchel, and Donatas Zigmantas. Revealing vibronic coupling in chlorophyll c1 by polarization-controlled 2d electronic spectroscopy. *Chemical Physics*, 530:110643, 2020.

[4] Tobias Brixner, Jens Stenger, Harsha M. Vaswani, Minhaeng Cho, Robert E. Blankenship, and Graham R. Fleming. Two-dimensional spectroscopy of electronic couplings in photosynthesis. *Nature*, 434(7033):625–628, 2005.

[5] Shaul Mukamel. Multidimensional femtosecond correlation spectroscopies of electronic and vibrational excitations. *Annual Review of Physical Chemistry*, 51(1):691–729, 2000.

[6] Rullière Claude. *Femtosecond laser pulses: principles and experiments.* Springer, 2005.

[7] Minhaeng Cho, Tobias Brixner, Igor Stiopkin, Harsha Vaswani, and Graham R. Fleming. Two dimensional electronic spectroscopy of molecular complexes. *Journal of the Chinese Chemical Society*, 53(1):15–24, 2006.

[8] Franklin D. Fuller and Jennifer P. Ogilvie. Experimental implementations of two-dimensional fourier transform electronic spectroscopy. *Annual Review of Physical Chemistry*, 66(1):667–690, 2015.

[9] L. Lepetit, G. Chériaux, and M. Joffre. Linear techniques of phase measurement by femtosecond spectral interferometry for applications in spectroscopy. *Journal of the Optical Society of America B*, 12(12):2467, 1995.

[10] Peter Hamm and Martin Zanni. *Concepts and methods of 2D infrared spectroscopy.* Cambridge University Press, 2011.

[11] David Palecek. *Quantum Coherence for Light Harvesting.* PhD thesis, Chemical Physics, 2015.

[12] Robert J. Silbey. Principles of nonlinear optical spectroscopy. *Journal of the American Chemical Society*, 118(50):12872–12872, 1996.

[13] Vytautas Butkus, Donatas Zigmantas, Leonas Valkunas, and Darius Abramavicius. Vibrational vs. electronic coherences in 2d spectrum of molecular systems. *Chemical Physics Letters*, 545:40–43, 2012.

[14] Lili Wang, Marco A. Allodi, and Gregory S. Engel. Quantum coherences reveal excited-state dynamics in biophysical systems. *Nature Reviews Chemistry*, 3(8):477–490, 2019.

[15] Jianshu Cao, Richard J. Cogdell, David F. Coker, Hong-Guang Duan, Jürgen Hauer, Ulrich Kleinekathöfer, Thomas L. C. Jansen, Tomáš Mančal, R. J. Dwayne Miller, Jennifer P. Ogilvie, and et al. Quantum biology revisited. *Science Advances*, 6(14), 2020.

[16] Mohan Srinivasarao. Nano-optics in the biological world: beetles, butterflies, birds, and moths. *Chemical Reviews*, 99(7):1935–1962, 1999.

[17] C. Shane. An introduction to electromagnetic wave propagation and antennas. *Choice Reviews Online*, 34(01), 1996.

[18] Charles H. Bennett and David P. Divincenzo. Quantum information and computation. *Nature*, 404(6775):247–255, 2000.

[19] Tomáš Mančal. Excitation energy transfer in a classical analogue of photosynthetic antennae. *The Journal of Physical Chemistry B*, 117(38):11282–11291, 2013.

[20] Claude Cohen-Tannoudji, Bernard Diu, Laloe Franck, Susan Reid Hemley, Nicole Ostrowsky, and D. B. Ostrowsky. *Quantum mechanics*. Wiley-VCH, 2020.

[21] Maximilian Schlosshauer. Decoherence, the measurement problem, and interpretations of quantum mechanics. *Reviews of Modern Physics*, 76(4):1267–1305, 2005.

[22] Wenxiang Hu, Bing Gu, and Ignacio Franco. Lessons on electronic decoherence in molecules from exact modeling. *The Journal of Chemical Physics*, 148(13):134304, 2018.

[23] Abraham Nitzan. *Chemical dynamics in condensed phases: relaxation, transfer and reactions in condensed molecular systems*. Oxford University Press, 2013.

[24] Shu-Hao Yeh, Ross D. Hoehn, Marco A. Allodi, Gregory S. Engel, and Sabre Kais. Elucidation of near-resonance vibronic coherence lifetimes by nonadiabatic electronic-vibrational state character mixing. *Proceedings of the National Academy of Sciences*, 116(37):18263–18268, 2018.

[25] Joachim Seibt, Thorsten Hansen, and Tõnu Pullerits. 3d spectroscopy of vibrational coherences in quantum dots: Theory. *The Journal of Physical Chemistry B*, 117(38):11124–11133, 2013.

[26] Hebin Li, Alan D. Bristow, Mark E. Siemens, Galan Moody, and Steven T. Cundiff. Unraveling quantum pathways using optical 3d fourier-transform spectroscopy. *Nature Communications*, 4(1), 2013.

[27] M. T. Zanni, N.-H. Ge, Y. S. Kim, and R. M. Hochstrasser. Two-dimensional ir spectroscopy can be designed to eliminate the diagonal peaks and expose only the crosspeaks needed for structure determination. *Proceedings of the National Academy of Sciences*, 98(20):11265–11270, 2001.

[28] Robin M. Hochstrasser. Two-dimensional ir-spectroscopy: polarization anisotropy effects. *Chemical Physics*, 266(2-3):273–284, 2001.

[29] Lars Olof Björn, George C. Papageorgiou, Robert E. Blankenship, and Govindjee. A viewpoint: Why chlorophyll a? *Photosynthesis Research*, 99(2):85–98, 2009.

[30] Stephen B. Klein. *Biology of plants*. W H Freeman, 2002.

[31] William G. Hopkins and Huner Normal P. A. *Introduction to plant physiology*. John Wiley and Sons, 2014.

[32] Martin Gouterman. Spectra of porphyrins. *Journal of Molecular Spectroscopy*, 6:138–163, 1961.

[33] Margus Rätsep, Juha Linnanto, and Arvi Freiberg. Mirror symmetry and vibrational structure in optical spectra of chlorophyll a. *The Journal of Chemical Physics*, 130(19):194501, 2009.

[34] K.k. Rebane and R.a. Avarmaa. Sharp line vibronic spectra of chlorophyll and its derivatives in solid solutions. *Chemical Physics*, 68(1-2):191–200, 1982.

[35] R.a. Avarmaa and K.k. Rebane. High-resolution optical spectra of chlorophyll molecules. *Spectrochimica Acta Part A: Molecular Spectroscopy*, 41(12):1365–1380, 1985.

[36] Ying Shi, Jian-Yong Liu, and Ke-Li Han. Investigation of the internal conversion time of the chlorophyll a from s3, s2 to s1. *Chemical Physics Letters*, 410(4-6):260–263, 2005.

[37] Elena Meneghin, Cristina Leonardo, Andrea Volpato, Luca Bolzonello, and Elisabetta Collini. Mechanistic insight into internal conversion process within q-bands of chlorophyll a. *Scientific Reports*, 7(1), 2017.

[38] Dariusz M. Niedzwiedzki and Robert E. Blankenship. Singlet and triplet excited state properties of natural chlorophylls and bacteriochlorophylls. *Photosynthesis Research*, 106(3):227–238, 2010.

[39] M. Fragata, B. Nordén, and T. Kurucsev. Linear dichroism(250–700 nm) of chlorophyll a and pheophytin a oriented in a lamellar phase of glycerylmonooctanoate/h2o. characterization of electronic transitions. *Photochemistry and Photobiology*, 47(1):133–143, 1988.

[40] Mitsuo Umetsu, Zheng-Yu Wang, Kenzi Yoza, Masayuki Kobayashi, and Tsunenori Nozawa. Interaction of photosynthetic pigments with various organic solvents 2. *Biochimica et Biophysica Acta (BBA) - Bioenergetics*, 1457(3):106–117, 2000.

[41] Martin Gouterman and Lubert Stryer. Fluorescence polarization of some porphyrins. *The Journal of Chemical Physics*, 37(10):2260–2266, 1962.

[42] M. E. Deroche and J. M. Briantais. Absorption spectra of chlorophyll forms, β-carotene and lutein in freeze-dried chloroplasts. *Photochemistry and Photobiology*, 19(3):233–240, 1974.

[43] Tohru Azumi and Kazuo Matsuzaki. What does the term "vibronic coupling" mean? *Photochemistry and Photobiology*, 25(3):315–326, 1977.

[44] John C. Tully. Perspective: Nonadiabatic dynamics theory. *The Journal of Chemical Physics*, 137(22), 2012.

[45] Jordan M. Womick and Andrew M. Moran. Vibronic enhancement of exciton sizes and energy transport in photosynthetic complexes. *The Journal of Physical Chemistry B*, 115(6):1347–1356, 2011.

[46] Ralph C. Dougherty, Harold H. Strain, Walter A. Svec, Robert A. Uphaus, and Joseph J. Katz. Structure, properties, and distribution of chlorophyll c. *Journal of the American Chemical Society*, 92(9):2826–2833, 1970.

[47] Donald R. Scott and Jean B. Allison. Solvent glasses for low temperature spectroscopic studies. *The Journal of Physical Chemistry*, 66(3):561–562, 1962.

[48] Donata's Zigmantas research group. 2d analysis, 2020.

[49] Tobias Brixner, Tomas Mancal, Igor V. Stiopkin, and Graham R. Fleming. Phase-stabilized two-dimensional electronic spectroscopy. *The Journal of Chemical Physics*, 121(9):4221–4236, 2004.

[50] David Palecek. Ft analysis, 2020.

[51] Infinite Studio LLC. Infinite design v. 3.4.21, 2020.

[52] David Palecek, Petra Edlund, Emil Gustavsson, Sebastian Westenhoff, and Donatas Zigmantas. Potential pitfalls of the early-time dynamics in two-dimensional electronic spectroscopy. *The Journal of Chemical Physics*, 151(2):024201, 2019.

[53] Vytautas Butkus, Jan Alster, Egle Basinskaite, Augulis Ramunas, Patrik Neuhaus, Leonas Valkunas, Harry L. Anderson, Darius Abramavicius, and Donatas Zigmantas. Discrimination of diverse coherences allows identification of electronic transitions of a molecular nanoring. *The Journal of Physical Chemistry Letters*, 8(10):2344–2349, 2017.

[54] Roberta Moca, Stephen R. Meech, and Ismael A. Heisler. Two-dimensional electronic spectroscopy of chlorophyll a: solvent dependent spectral evolution. *The Journal of Physical Chemistry B*, 119(27):8623–8630, 2015.

[55] N. Michniewicz, A.s. Muszyński, W. Wrzeszcz, M.a. Czarnecki, B. Golec, J.p. Hawranek, and Z. Mielke. Vibrational spectra of liquid 1-propanol. *Journal of Molecular Structure*, 887(1-3):180–186, 2008.

[56] David Paleček, Petra Edlund, Sebastian Westenhoff, and Donatas Zigmantas. Quantum coherence as a witness of vibronically hot energy transfer in bacterial reaction center. *Science Advances*, 3(9), 2017.

[57] Erling Thyrhaug, Craig N. Lincoln, Federico Branchi, Giulio Cerullo, Václav Perlík, Frantisek Sanda, Heiko Lokstein, and Jürgen Hauer. Carotenoid-to-bacteriochlorophyll energy transfer through vibronic coupling in lh2 from phaeosprillum molischianum. *Photosynthesis Research*, 135(1-3):45–54, 2017.